Balmer-Dominated Spectra of Nonradiative Shocks in the Cygnus Loop, RCW 86 and Tycho Supernova Remnants

Parviz Ghavamian[1,3,5], John Raymond[2], R. Chris Smith[4] and Patrick Hartigan[1]

Received _____; accepted _____

Accepted by the Astrophysical Journal

ABSTRACT

We present an observational and theoretical study of the optical emission from nonradiative shocks in three supernova remnants: the Cygnus Loop, RCW 86 and Tycho. The spectra of these shocks are dominated by collisionally excited hydrogen Balmer lines which have both a broad component caused by proton-neutral charge exchange and a narrow component caused by excitation of cold neutrals entering the shock. In each remnant we have obtained the broad to narrow flux ratios of the Hα and Hβ lines and measured the Hα broad component width.

A new numerical shock code computes the broad and narrow Balmer line emission from nonradiative shocks in partially neutral gas. The Balmer line fluxes are sensitive to Lyman line trapping and the degree of electron-proton temperature equilibration. The code calculates the density, temperature and size of the postshock ionization layer and uses a Monte Carlo simulation to compute narrow Balmer line enhancement from Lyman line trapping. The initial fraction of the shock energy allocated to the electrons and protons (the equilibration) is a free parameter. Our models show that variations in electron-proton temperature equilibration and Lyman line trapping can reproduce the observed range of broad to narrow ratios. The results give 80%$-$100% equilibration in nonradiative portions of the NE Cygnus Loop ($v_S \sim 300$ km s^{-1}), 40%$-$50% equilibration in nonradiative portions of RCW 86 ($v_S \sim 600$ km s^{-1}) and $\lesssim 20\%$ equilibration in Tycho ($v_S \sim 2000$ km s^{-1}). Our results suggest an inverse correlation between magnetosonic Mach number and equilibration in the observed remnants.

Subject headings: ISM: supernova remnants: shock waves, radiative transfer

[1]Department of Space Physics and Astronomy, Rice University, 6100 S. Main St., Houston, TX, 77005−1892; hartigan@sparky.rice.edu

[2]Harvard-Smithsonian Center for Astrophysics, 60 Garden St., Cambridge, MA 02138; raymond@cfa.harvard.edu

[3]Current address: Department of Physics and Astronomy, Rutgers University, 136 Frelinghuysen Road, Piscataway, NJ 08854-8019; parviz@physics.rutgers.edu

[4]Cerro Tololo Inter-American Observatory, Casilla 603, Chile; csmith@noao.edu

[5]Visiting Astronomer, Cerro Tololo Inter-American Observatory, National Optical Astronomy Observatories. CTIO is operated by AURA, Inc. under contract to the National Science Foundation.

1. INTRODUCTION

Supernova explosions produce some of the strongest shocks in nature. During the event, the outer layers of a star are ejected at speeds as high as 30,000 $\mathrm{km\,s^{-1}}$. The dense ejecta behave like a highly supersonic piston, producing a strong shock wave in the ISM ahead of the piston (commonly known as the forward shock). When the mass swept up by the forward shock begins to exceed the ejecta mass, the supernova remnant (SNR) enters the blast wave (Sedov-Taylor) phase of evolution (Hamilton & Sarazin 1984, Truelove & McKee 1999). From the genesis of the SNR through the blast wave stage the forward shock is nonradiative, meaning that it loses a negligible fraction of its internal energy to radiative cooling.

Due to the low density ($\mathrm{n} \lesssim 1$ $\mathrm{cm^{-3}}$) and high Mach number ($M \gtrsim 200$) of the forward shock, the heated interstellar gas behaves like a collisionless plasma (Draine & McKee 1993). According to the strong shock jump conditions, electrons and protons are heated to temperatures in a minimum ratio $T_e/T_p = m_e/m_p\,(\sim 1/2000)$. However, plasma waves and MHD turbulence at the shock front may transfer energy from protons to electrons (Tidman & Krall 1971, Kennel 1985, Cargill & Papadapoulos 1988), further equilibrating the two particle temperatures. Since the electrons and protons are affected by a different range of plasma waves and the Coulomb equilibration time downstream often exceeds the age of the remnant, the two particle temperatures can remain unequal throughout the shock. The types of plasma waves excited at the shock transition (and hence the amount of collisionless heating) depend strongly on parameters such as the magnetosonic Mach number M_S and magnetic field orientation. Due to this complicated dependence and the extreme difficulty of creating high Mach number collisionless shocks in the laboratory, the properties of collisionless shocks remain poorly understood.

In a cold ($\lesssim 10^4$ K), partially ionized medium, the charged and neutral distributions respond very differently to the passage of a collisionless shock. The cold neutrals are initially unaffected by the shock transition, while charged particles are compressed by a factor of four and strongly heated. Some of the cold neutrals entering the shock are collisionally excited before being destroyed by collisional ionization or charge transfer. Radiative decay by these excited neutrals

produces narrow component Balmer emission with a line width given by the preshock temperature. In contrast, charge exchange between cold neutrals and protons produces fast neutrals having the velocity distribution of the postshock protons. Collisional excitation of the fast neutrals produces broad Balmer line emission (Chevalier & Raymond 1978, Chevalier, Kirshner & Raymond 1980 (hereafter CKR80)). While the low temperatures in radiative shocks favor the emission of strong forbidden lines such as [O II], [O III], [N II] and [S II], the high temperatures behind nonradiative shocks produce hydrogen Balmer line emission far more efficiently. Balmer-dominated shocks have been detected in Tycho (Kirshner, Winkler & Chevalier 1987 (hereafter KWC87), Smith *et al.* 1991, Ghavamian *et al.* 2000), SN 1006 (KWC87, Smith *et al.* 1991, Winkler & Long 1997), RCW 86 (Long & Blair 1990, Smith 1997), Kepler (Blair, Long & Vancura 1991), portions of the Cygnus Loop (Raymond *et al.* 1983 (hereafter RBFG83), Fesen & Itoh 1985, Hester, Raymond & Blair 1994 (hereafter HRB94)), four remnants in the LMC (Tuohy *et al.* 1982, Smith *et al.* 1991, 1994) and the bow shock surrounding the pulsar PSR 1957+20 (Aldcroft, Romani & Cordes 1992).

The optically emitting layer behind a nonradiative shock is extremely thin ($\lesssim 10^{-3}$ pc), so the proton temperature very close to the shock front can be measured from the width of a broad Balmer line. The proton temperature in turn depends on the shock velocity through the jump conditions, making the broad line profile a powerful diagnostic for probing the global kinematics of young SNRs. The broad to narrow flux ratio is another important diagnostic because it also depends on the shock velocity (CKR80, Smith *et al.* 1991). Proper motion measurements of Balmer-dominated filaments have been combined with shock velocity estimates from the broad component to estimate distances to several young SNRs (for example see Long, Blair & van den Bergh 1988 for SN 1006, and Hesser & van den Bergh 1981 for Tycho).

Balmer-dominated spectra can be difficult to interpret because the broad component width and broad to narrow ratio yield different shock velocities depending on the assumed electron-proton equilibration. Since the equilibration is not known a priori, spectroscopic observations in the past have only yielded a range of shock velocities v_S from the Balmer line profiles: a minimum $v_S(min)$ for no equilibration and a maximum $v_S(max)$ for full equilibration. In addition, collisional

excitation behind the shock generates both Lyman line photons and Balmer line photons. Lyman line trapping by slow neutrals partially converts Ly β and higher Lyman photons into Balmer line photons; this enhances the Balmer line flux in the narrow component and complicates the diagnostic interpretation of the broad to narrow ratio (CKR80, Smith *et al.* 1991, Ghavamian 1999)). Moreover, since the Ly β optical depth is larger than that of Ly γ, the Hα broad to narrow ratio is more strongly affected than the Hβ broad to narrow ratio. The Lyman line optical depth behind the shock typically lies between 0 and 1, so that neither Case A nor Case B conditions apply. It is clear that disentangling the combined effects of Lyman line trapping and equilibration on a Balmer-dominated spectrum requires (1) the acquisition of high S/N line profiles in both Hα and Hβ, and (2) careful modeling of the atomic physics and radiative transfer.

In §2 of this paper, we present high S/N spectra of three nonradiative shocks which resolve the broad and narrow components of both Hα and Hβ. In §3, we present measurements of the Hα broad component width and broad to narrow ratios in Hα and Hβ. We describe numerical models of nonradiative shocks in §4, including calculations of ionization structures for a range of equilibrations and Monte Carlo simulations of Ly β and Ly γ trapping. In §5 we compare the observed broad to narrow ratios with model predictions and simultaneously determine both the shock velocity and equilibration for the observed SNRs. In §6 we discuss our results and in §7 we present our conclusions.

2. SPECTROSCOPIC OBSERVATIONS

The spectroscopic datasets presented here were acquired over a one year period between October 1997 and September 1998. We chose the instrumental setup for each observation to simultaneously maximize the number of detected photons and provide enough spectral resolution to separate the broad Balmer lines from the narrow Balmer lines. A log of our spectroscopic observations appears in Table 1. The telescope and spectrograph configurations used for the observations are described below.

2.1. Cygnus Loop and Tycho

Our spectroscopic observations of NE Cygnus and Tycho were performed on the nights of October 7-10, 1997 (UT), using the 1.5 meter Tillinghast reflector telescope at the Fred Lawrence Whipple Observatory. The Schmidt camera CCD was a Loral 512×2688 pixel chip, with an unbinned plate scale of $0.6''$ per 15μm pixel. To reduce readout noise during these observations, we binned the CCD chip by 4 pixels along the spatial direction. The spectrograph was equipped with a 1200 l mm^{-1} grating blazed at 5700 Å, providing a dispersion of 0.38 Å pixel^{-1} and spectral coverage of 1000 Å. With this setup, only one Balmer line could be fit on the CCD chip, so we performed the Hα and Hβ observations at different times. Our target in NE Cygnus Loop was filament P7 from the list of positions observed by the Hopkins Ultraviolet Telescope during the Astro-2 mission. We used a $1.1'' \times 3'$ slit for Hα, yielding a resolution of 1.4 Å. To obtain the Hβ line profile, we observed Cygnus P7 again on the night of September 26, 1998 (UT). In this case, we used a $3'' \times 3'$ slit with the 1200 l mm^{-1} grating, yielding a resolution of 1.5 Å. A POSS image of the Cygnus P7 filament appears in Figure 1, along with the two-dimensional FAST spectrum. The one-dimensional Hα and Hβ profiles appear in Figure 2. From the Hα line, we find a broad component width of 262±32 km s^{-1}, with no evidence of forbidden line emission. The shift between the broad and narror component line centers is less than the uncertainty in broad component width, indicating a nearly edge-on viewing geometry.

The 1997 Tycho observations focused on the bright nonradiative shock Knot g. In these observations, we used the 300 l mm^{-1} grating with a $3''$ slit, centered on 5545 Å (4000 Å coverage). This convenient combination put both Hα and Hβ on the CCD chip and allowed simultaneous detection of the Hα and Hβ broad components. As in the previous observations, we binned the CCD chip by 4 pixels. The resolution for this setup was 275 km s^{-1} (6 Å at Hα). It is evident from the two-dimensional spectrum (Figure 3) that the Hα surface brightness and broad component width vary with position along the Knot g filament, reflecting variations in preshock density, shock velocity and viewing angle. The extraction aperture shown in Figure 3 was centered on the upper part of Knot g, where the broad component is brightest and its width most nearly

constant (hereafter labeled Knot g (1)). The extracted Hα and Hβ line profiles appear in Figure 4. Knot g (1) is the brightest portion of the filament (broad component FWHM of 1765±110 km s^{-1}), while the lower part Knot g (2) is fainter (broad FWHM of 2105±130 km s^{-1}). The broad component center of Knot g (1) is redshifted 132±35 km s^{-1} from the center of the narrow component, indicating that the plane of the shock is tilted slightly into the plane of the sky.

In the 1997 Tycho spectra, we detected faint diffuse Hα emission above Knot g. We did not subtract the 1-D diffuse spectrum directly from that of Knot g (1) because then the resulting 1-D spectrum becomes too noisy to detect the Hβ broad component. Instead, we measured the Hα surface brightnesses of Knot g and the diffuse emission separately, using FAST spectra acquired in 1998 (using the same detector setup as the 1997 observations, see Ghavamian *et al.* 2000). From the 1998 data, we found that the Diffuse Hα emission contributes approximately 12% of the narrow flux from Knot g (1). We have used this information to correct the Hα broad to narrow ratio of Knot g (1). The diffuse Hβ emission is very faint and is almost lost in the noise, so we have not corrected the Hβ broad to narrow ratio. In a separate paper (Ghavamian *et al.* 2000), we show that the diffuse emission is associated with a photoionization precursor from the supernova blast wave. Since the width of the broad Hbeta line and its shift from zero velocity must be the same as from the high S/N Hα measurement, we hold these quantities fixed while simultaneously fitting the broad and narrow Hβ lines. Constraining the fit in this manner is useful because the S/N of the Hβ broad component is signifcantly lower than that of Hα.

Prior to our observations, the most recent spectroscopic study of Knot g was that of Smith *et al.* (1991), who found a broad FWHM of 1900±300 in Hα. This value was obtained by averaging the broad component width over the length of Knot g. We note that this velocity lies roughly midway between our separately measured broad component widths for sections (1) and (2). In addition, the average Hα broad to narrow ratio of sections (1) and (2) lies within the range quoted by Smith *et al.* (1991). However, in our spectra we find a significantly smaller shift in the broad component line center than Smith *et al.* (1991). This may be due to the strong variations in shock viewing angle along the length of the filament. In Table 2 we present our observational

results for Knot g side by side with those of earlier papers.

Since the Hα and Hβ lines were recorded simultaneously, we were able to measure the broad and narrow component Balmer decrements $I_{H\alpha}/I_{H\beta}$ separately for Knot g (1). Although the S/N of the broad Hβ line is significantly lower than that of the broad Hα line, we were able to estimate the broad Hβ flux by setting the width and center of this line equal to that of Hα during fitting. The Balmer decrements are shown in Table 3 for the broad and narrow components of Tycho Knot g (1). For comparison, we have computed $I_{H\alpha}/I_{H\beta}$ for both upper and lower limits of the visual extinction parameter ($1.6 \leq A_V \leq 2.6$) determined by CKR80. It is evident that the narrow Balmer decrement is considerably larger than the broad Balmer decrement. Interestingly, using $A_V = 1.6$ yields a broad Balmer decrement of 3.67, consistent with pure collisional excitation in a high temperature ($\gtrsim 10^6$ K) gas. Adopting the smaller value of A_V also results in better agreement between observations and models of the photoionization precursor (Ghavamian *et al.* 2000).

2.2. RCW 86

We observed the galactic SNR RCW 86 on April 5-8, 1998 (UT), using the RC Spectrograph at the f/7.8 focus of the CTIO 4 meter telescope. The RC Spectrograph features a Loral 3k CCD with 15μm pixels connected to a Blue Air Schmidt camera. This combination gives a plate scale of $0.5''$ pixel^{-1}. A decker allows for an adjustable slit length, with a maximum unvignetted slit size of $5'$. Our observations targeted 4 positions around the remnant, and included moderate resolution spectra of the Hα and Hβ lines. In the Hα observations, we used the CTIO 1200 l mm^{-1} grating (0.5 Å pixel^{-1}, blazed at 8000 Å) with a filter inserted to exclude higher order emission lines. With a $3''$ slit, the spectral resolution of the Hα observations was 2.2 Å, with spectral coverage of 1565 Å. To obtain the Hβ line profiles, we used the 860 l mm^{-1} grating in 2nd order (0.34 Å pixel^{-1}, blazed at 5500 Å), with filter bg39 to exclude higher order emission lines. Combined with a slit size of $3''$, the resolution of the Hβ setup was 1.4 Å, with spectral coverage of 1135 Å.

The brightest nonradiative shocks in RCW 86 are located in the southwestern corner of the

remnant, flanking the bright radiative shocks (Figure 5). From the two-dimensional spectrum of SW RCW 86, it is evident that some of the shocks at this location have become radiative (marked by the absence of broad Balmer emission and the presence of [N II] $\lambda\lambda$6548, 6583 and [S II] $\lambda\lambda$6716, 6731 lines). We centered the extraction aperture as shown in Figure 5 to avoid the radiative emission above and bright stellar continuum below the aperture. Both optical (Leibowitz & Danziger 1983, Rosado *et al.* 1996, Smith 1997)) and X-ray (Kaastra *et al.* 1992, Smith 1997, Vink, Kaastra & Bleeker 1998, Petruk 1999) observations have shown that the radiative emission arises from a dense cloud overrun by the supernova blast wave. The high neutral density is also responsible for the brightness of the broad and narrow Hα lines in the one-dimensional spectrum (Figure 6).

We reduced all spectroscopic data using standard routines in IRAF[6]. After applying overscan, bias, flat field, response and dark count corrections to all two-dimensional spectra, we corrected for the slit function in the two-dimensional spectra using twilight sky flights. Finally, we untilted the emission lines using wavelength solutions from calibration lamp spectra, then subtracted the sky background using night sky emission adjacent to each target object.

The spectra presented in this paper were acquired under varying photometric conditions. Skies where non-photometric during the 1997 observations, so we only applied a sensitivity correction to the Cygnus Loop and Tycho data. Throughout the 1998 observations, however, conditions at Mt. Hopkins were nearly photometric. Comparison of the spectra from standard stars Hiltner 102, LB 1240, HD 192281 and BD 284211 with one another indicates that the 1998 Cygnus Loop spectrum is photometrically accurate to within 20%. The Hα observations of RCW 86 were performed under nearly photometric conditions, while the Hβ observations were performed under partial cirrus. From an examination of spectra from standard stars LTT 3218, LTT 7379 and LTT 7987, we estimate that the Hα flux shown in Figure 6 is accurate to within 10%.

[6]IRAF is distributed by the National Optical Astronomy Observatories, which is operated by the AURA, Inc. under cooperative agreement with the National Science Foundation

3. Line Profile Fits

To extract the broad and narrow component fluxes and measure the width of the broad component, we fit each Balmer line profile with two independent Gaussians plus a linear background. Using the IRAF deblending task SPLOT and self-written routines for χ^2 minimization fitting, we obtained quantitative estimates of the line flux, width and center of the broad and narrow Balmer lines. Since the position of the zero level background affects the estimated flux of the broad component, this baseline uncertainty is the dominant source of nonrandom error in cases where the broad component is very wide and faint (as in Tycho, for example). Both the baseline uncertainty and statistical uncertainty have been included in the quoted broad to narrow ratios.

We measured the broad component widths from the Hα line profiles, then corrected for the instrumental response by subtracting the narrow component width in quadrature from the broad component width. In each case, the narrow component widths were equal to the instrumental resolution (they were unresolved). The broad and narrow components are most tightly blended in the Cygnus P7 line profiles. The error bars on the Hα and Hβ broad to narrow ratios are correspondingly larger.

4. The Numerical Shock Models

The goal of the numerical models is to calculate the Hα and Hβ broad to narrow ratios for arbitrary shock speed, equilibration and preshock neutral density. Comparing the predicted broad to narrow ratios with the observed values should then allow us to constrain the shock velocity and equilibration of the observed SNRs. To compute the Balmer line flux from a nonradiative shock, we have computed the density and temperature of the postshock gas as a function of position. We have used the results of these calculations to compute the Ly β and Ly γ optical depths behind the shock. The Lyman optical depth behind the shock typically lies between 0 and 1, meaning that neither Case A nor Case B conditions apply.

4.1. Cross Sections

We have consulted the following sources for collision cross sections and strengths:

Collisional Ionization and Charge Exchange: In the shock models we use the polynomial fit to the electron-hydrogen ionization cross section from Janev *et al.* (1987). The proton ionization cross section is from a numerical fit by Janev *et al.* that reproduces the experimental data of Shah *et al.* (1998), Shah, Elliott & Gilbody (1987) and Shah & Gilbody (1981) to within their uncertainties. The $H-H^+$ charge exchange rate used in the shock code has been taken from the analytic fit of Freeman & Jones (1974).

Collisional Excitation: For electron temperatures below 5×10^5 K, we use the polynomial fits of Giovanardi, Natta & Palla (1987) to the $3s, p, d$ and $4s, p, d, f$ collision strengths. Above 5×10^5K, we compute the collision rates directly using the modified Born approximation cross sections of Whelan (1986). The available data on proton excitation is relatively sparse in the literature, and theoretical cross sections to $n = 3$ and 4 have only recently become available. The close-coupling calculations by Martín (1999) include cross sections to fine structure levels of $n = 3$ and 4 for proton energies above 40 keV. The calculations of Martín include charge exchange into excited states, a process which contributes as much as 20% to the Balmer line flux at high shock velocities ($v_S \gtrsim 1500$ km s^{-1}). The theoretical values agree reasonably well with the experimental measurements of Detleffsen *et al.* (1994), which covered proton energies in the range 40 keV$\leq E \leq$800 keV. The shock code utilizes the cross sections of Martín (1999) and uses the calculations of McLaughlin *et al.* (1998) to estimate excitation cross sections between 10 and 40 keV.

4.2. Ionization Structures

The shock structure calculation is initiated by using the jump conditions to set the temperature and density at the first time step. The equations describing the number densities of slow neutrals, fast neutrals, electrons and protons form a set of coupled, linear differential

equations which can be solved together to calculate the density of each species behind the shock. Assuming a pure H plasma ($n_e = n_p$), the equation for the slow neutrals is

$$\frac{dn_{H^0}(s)}{dt} = -\,n_e\,n_{H^0}(s)\,(\langle\sigma_i v\rangle_e^s + \langle\sigma_i v\rangle_p^s + \langle\sigma_{cx} v\rangle^s) \tag{1}$$

where $\langle\sigma_i v\rangle_{e,p}^s$ and $\langle\sigma_{cx} v\rangle^s$ are the electron/proton ionization coefficients and H−H$^+$ charge exchange coefficients for slow neutrals (in cm^3 s^{-1}), and n is the number density (cm^{-3}) of a given particle species. Solving this equation for $n_{H^0}(s)$, the slow neutral density at time step $t_j\,(= t_{j-1} + \Delta t)$ is

$$n_{H^0}^j(s) = n_{H^0}^{j-1}(s)\,e^{-n_e^{j-1}\,(\langle\sigma_i v\rangle^s + \langle\sigma_{cx} v\rangle^s)\,\Delta t} \tag{2}$$

where $\langle\,\sigma_i v\rangle^s = \langle\,\rangle_e + \langle\,\rangle_p$ is the total ionization coefficient due to protons and electrons evaluated at t_j. The relation for fast neutrals is

$$n_{H^0}^j(f) = n_{H^0}^{j-1}(f)\,e^{-(n_e^{j-1}\,\langle\sigma_i v\rangle^f\,\Delta t)} + 4\,n_{H^0}^{j-1}(s)\,e^{-(n_e^{j-1}\,\langle\sigma_i v\rangle^s\,\Delta t)}\,(1 - e^{-(n_e^{j-1}\,\langle\sigma_{cx} v\rangle^s\,\Delta t)}) \tag{3}$$

where $\langle\,\rangle^f$ represents the collision rate coefficient for electrons or protons and fast neutrals. In the above equation, the first term represents the loss of fast neutrals by ionization, while the second term represents the increase of fast neutrals by charge exchange (the factor of 4 takes into account the compression behind a strong shock). Mass conservation requires that the electron and proton number densities increase in proportion to the ionization rate; therefore the equations for $n_{H^0}(s)$ and $n_{H^0}(f)$ can be used to calculate the proton density:

$$n_p^j = n_e^j = n_p^{j-1} + 4\,n_{H^0}^{j-1}(s)\,(1 - e^{-(n_e^{j-1}\,\langle\sigma_i v\rangle^s\,\Delta t)}) + n_{H^0}^{j-1}(f)\,(1 - e^{-(n_e^{j-1}\,\langle\sigma_i v\rangle^f\,\Delta t)}) \tag{4}$$

Two important complications arise in the collision rate calculations for a nonradiative shock. First, $T_e \neq T_p$ just behind the shock so that the electron and proton temperatures change continually with position as Coulomb collisions attempt to establish equilibrium. Hence, the collision rate coefficients also evolve with position and must be computed for a range of electron and proton temperatures. Second, since the slow neutrals are unaffected by the shock, they encounter an anisotropic proton distribution which is bulk shifted to $\frac{3}{4}\,v_S$ (CKR80, Smith *et al.* 1991). Slow neutrals can also encounter an anisotropic electron distribution if the plasma is

far from temperature equilibrium and the postshock bulk velocity is comparable to the electron thermal speed.

Another important complication occurs when the temperatures of the electrons and fast neutrals are unequal. For the case $T_e = T_p$ (equilibrated plasma), the electron thermal speed is 43 times higher than the fast neutral thermal speed (= proton thermal speed). The fast neutrals are effectively at rest relative to the electrons, and the ionization rate integral is simple to evaluate. However, for an unequilibrated case, the collision rate integral involves the distribution functions of both electrons and fast neutrals, and becomes a complicated 6-dimensional integral over the velocities of both species (Smith *et al.* 1991). Fortunately, the electron-fast neutral collision rate integrals can be reduced to one-dimensional form involving the relative speed of the two particle species (Bandiera, 1998; Weisheit, 1998). Throughout the shock code, we have computed the electron-fast neutral and electron-slow neutral rates using the reduced integral.

As mentioned earlier, electrons and protons behind a nonradiative shock can be heated to very different fractions of the bulk flow energy. The total thermal energy E_{tot} acquired by the postshock gas is, however, constant:

$$E_{tot} = \frac{3}{16}(m_e + m_p)\, v_S^2 \approx \frac{3}{16}\, m_p\, v_S^2 \tag{5}$$

The *initial* fraction of this energy going into electrons and protons is controlled by collisionless heating at the shock front, and is therefore a free parameter. Let us define the parameter f_{eq} such that $f_{eq} = 0$ for no initial electron-proton equilibration and $f_{eq} = 1$ for full initial electron-proton equilibration. The postshock temperatures for arbitrary f_{eq} are then

$$T_p = T_{0p} + \frac{1}{2}\frac{3}{16}(m_e\, f_{eq} + (2 - f_{eq})\, m_p)\frac{v_S^2}{k} \tag{6}$$

and

$$T_e = T_{0e} + \frac{1}{2}\frac{3}{16}(m_p\, f_{eq} + (2 - f_{eq})\, m_e)\frac{v_S^2}{k} \tag{7}$$

where $T_{0p,e}$ are the preshock proton and electron temperatures, respectively. For the extreme cases of no equilibration and full equilibration,

$$T_{p,e} = T_{0p,e} + \frac{3}{16}\frac{m_{p,e}}{k}\, v_S^2 \quad (f_{eq} = 0) \tag{8}$$

and

$$T_{p,e} = T_{0p,e} + \frac{1}{2}\frac{3}{16}\frac{(m_e + m_p)}{k} v_S^2 \approx T_{0p,e} + \frac{1}{2}\frac{3}{16}\frac{m_p}{k} v_S^2 \quad (f_{eq} = 1) \tag{9}$$

The temperature of the preshock medium is generally low enough so that $T_{0p} = T_{0e} (= T_0)$. The initial ratio of T_e/T_p behind the shock can be obtained by dividing Equations 7 and 6. Assuming that T_{0p} and T_{0e} are small enough to ignore,

$$\frac{T_e}{T_p} \approx \frac{f_{eq}}{2 - f_{eq}} \tag{10}$$

where terms involving m_e/m_p have been dropped. A diagram showing the dependence of T_e and T_p on v_S and f_{eq} appears in Figure 7.

To illustrate the dependence of postshock ionization structures on the shock velocity and equilibration, we now describe four numerical models (assuming preshock parameters $n_0 = 1$ cm^{-3}, $f_{H^0} = 0.5$, $T_0 = 5{,}000$ K):

250 and 500 km s^{-1}: The postshock electron and proton temperatures equilibrate rapidly in the 250 km s^{-1} model, even when $f_{eq} = 0$. The protons are too cold to appreciably ionize H, so charge transfer and electron collisions dominate the ionization balance of the postshock gas. The slow and fast neutral densities are shown as a function of position behind the shock in Figure 8. Coulomb collisions in the 500 km s^{-1}, $f_{eq} = 0$ model only produce 30% equilibration by the time the neutrals fully ionize, and once again charge exchange is the dominant interaction between protons and neutral atoms. In this model, the broad and narrow Balmer emission is produced well before equilibration is complete. Note that the ionization zones for both 250 km s^{-1} and 500 km s^{-1} models are more extended for low equilibration than for high equilibration. At higher equilibrations the electrons are hotter, ionizing the gas more efficiently and reducing the thickness of the postshock neutral layer. At fixed equilibration, the size of the neutral layer is proportional to the shock velocity. Therefore, the faster the flow, the larger the neutral layer.

1500 and 2500 km s^{-1}: There are two important differences between these models and those at lower shock velocity. First, T_p in a high velocity $f_{eq} = 0$ shock starts off so much higher than T_e that electron-proton equilibration is only a few percent complete by the time all the neutrals

disappear and all the Balmer emission is produced. Second, the proton ionization rate is now comparable to the electron ionization rate, and a sizable fraction of the Balmer line emission is produced by proton excitation. At these shock velocities, the proton-slow neutral collision rate is a factor of 2 or more higher than the proton-fast neutral collision rate, due to the bulk velocity-shifted proton distribution encountered by the slow neutrals. At fixed shock velocity, the size of the postshock ionization layer is larger for high equilibration than low equilibration (Figure 8), the opposite of the 250 and 500 $\mathrm{km\,s^{-1}}$ models.

4.3. Calculation of Broad FWHM vs. Shock Velocity

To make the best use of the observational data, we have used the broad component Hα widths in each SNR to bracket the range of possible shock velocities. For a given broad component width, no equilibration (f_{eq} =0) yields the smallest shock velocity $v_S(min)$, while full equilibration (f_{eq} =1) yields the largest shock velocity v_{max} (CKR80, Smith 1991). Intermediate equilibrations yield intermediate v_S. For each observed shock, we ran numerical models sampling a range of f_{eq} between 0 and 1, with each value of f_{eq} mapping onto a unique v_S. We then compared the output Hα and Hβ broad to narrow ratios with the observed values. In this manner, our models self consistently utilized all of the relevant observables from each Balmer line spectrum.

For a given broad FWHM, the map between f_{eq} and v_S is the line profile function $\phi(v_x)$ (Smith *et al.* 1991, CKR80). For a plane parallel shock viewed edgewise, $\phi(v_x)$ is defined as the number of fast neutrals with velocity v_x along the line of sight:

$$\phi(v_x) \;=\; \frac{l_p^3}{\pi^{3/2}\,(\langle\sigma_{cx}v\rangle^s + \langle\sigma_i v\rangle^s)}\, e^{-l^2 v_0^2} \int_{-\infty}^{\infty}\int_{-\infty}^{\infty} v\,\sigma_{cx}(v)\, e^{-l^2\,(v^2\,-\,2\,v_0\,v_z)}\, dv_y\, dv_z \qquad (11)$$

where $v^2 = v_x^2 + v_y^2 + (v_z - v_0)^2$, $l_p = (m_p/2kT_p)^{1/2}$ and $v_0 = \frac{3}{4}v_S$ is the bulk velocity of the shocked gas, taken to be along the z axis. We have computed $\phi(v_x)$ numerically for a range of f_{eq} and v_S. In Figure 9 we present plots of the expected FWHM vs. shock velocity for four equilibrations. We have used these results to estimate v_S for the observed nonradiative shocks,

listed in Table 4 for the limits of no equilibration and full equilibration.

4.4. Monte Carlo Models of Ly β and Ly γ Trapping

With the densities and temperatures of different particle species known for a given v_S and f_{eq}, we can now quantitatively estimate the contribution of Lyman line trapping to the Hα and Hβ lines. Since Lyman photons are emitted with Doppler shifts randomly distributed over the line profile, it is possible for a Lyman photon generated near line center of a fast neutral to be absorbed by a slow neutral, and vice versa. The conversion of Lyman line photons to Balmer line photons depends on the likelihood of absorption. Due to the $\frac{3}{4}\,v_S$ velocity shift between fast and slow neutrals, the optical depth depends on both the frequency and direction of an emitted Lyman photon. Therefore, our radiative transfer calculation follows the propagation, absorption and conversion of individual Lyman photons behind the shock.

We model the conversion of Lyman photons into Balmer photons using a Monte Carlo simulation. Lyman photons are propagated through the shock until they are either converted into Balmer photons or escape from the grid. Due to the large Doppler motions of fast neutrals, most of the broad Lyman photons escape from the shock. Narrow Lyman photons, on the other hand, can be absorbed both behind and ahead of the shock. There is effectively an infinite optical depth to narrow component Lyman photons in the preshock region; some absorption occurs even if the preshock neutral density is very small (CKR80). For this reason, the radiative transfer calculation includes the preshock region, where the temperature and density are assumed constant.

The Monte Carlo program used in this work is based on an earlier code used by HRB94, with atomic data updated to include Hβ emission and proton excitation. The probability that a Lyman photon will be absorbed at each point in the grid depends on the optical depth τ_ν at each point. The optical depth, in turn, depends on the random velocity of the emitting atom along the direction of emission, and whether the atom is a fast or slow neutral. In the Monte Carlo program, 10,000 individual photons are generated with random Doppler shifts, randomly distributed behind

the shock according to the emissivity. If a given excitation produces a Lyman photon, the photon is followed along a randomly oriented ray until it is either converted into a Balmer photon or escapes from the grid. After 10,000 excitations, the number of accumulated broad and narrow Balmer photons is divided to obtain the broad to narrow intensity ratio.

Before we compare our models with the observations, we note that our predicted broad to narrow ratios offer a number of improvements over previous calculations (such as those of HRB94). The current models utilize more recent atomic rates and compute the broad to narrow ratios for both Hα and Hβ. Our new models also include direct collisional excitation of hydrogen by protons. Finally, by arranging our models into a grid we have been able to predict broad to narrow ratios for a single set of models covering a wide range of shock velocities and equilibrations.

5. Comparison of Models and Observations

With the numerical models available, we can now estimate v_S and f_{eq} for Cygnus P7, SW RCW 86 and Tycho Knot g (1). There is observational evidence that the temperature ahead of nonradiative shocks can be as high as 40,000 K (Ghavamian *et al.* 2000, Smith *et al.* 1994, HRB94). The model predictions are rather insensitive to the preshock temperature (the Lyman optical depth at line center $\propto T^{-1/2}$), so in the following sections we have set T_0 =5,000 K in all models. It should also be noted that since the preshock neutral density is equal to the neutral fraction times the total preshock density ($n_{H^0} = f_{H^0}\, n_0$), predicted broad to narrow ratios from models with high f_{H^0} and low n_{H^0} are similar to models with low f_{H^0} and high n_0. The reasons for this property are that (1) the total preshock density scales out of the ratio of the broad to narrow Lyman line optical depths, and (2) the equilibration, ionization and charge exchange times behind the shock scale as $1/n_0$, offsetting the influence of varying n_0 on the excitation/ionization rates. Along with v_S and f_{eq}, the preshock neutral fraction f_{H^0} is the most important quantity affecting the broad to narrow ratios. For this reason, we set $n_0 = 1$ cm^{-3} in the models which follow.

5.1. Cygnus Loop P7

To interpret our results we ran numerical shock models using the fractional equilibrations f_{eq} =0, 0.03, 0.05, 0.2, 0.5, 0.8 and 1.0, along with their corresponding shock velocities of 265, 268, 270, 273, 296, 332 and 365 km s^{-1}. The predicted Hα and Hβ broad to narrow ratios are shown in Figure 10 vs. equilibration for preshock ionization fractions of 0.1, 0.5 and 0.9. In these models, the total preshock density is 1 cm^{-3}. Each curve in the figure corresponds to a different preshock neutral fraction f_{H^0}. Each point along a given curve corresponds to a different equilibration and maps to a different shock velocity. An outstanding feature of the models is that the broad to narrow ratios reach a maximum at low equilibration. The peak occurs because the broad to narrow ratios are proportional to the ratio of the charge exchange rate to the collisional ionization rate. In these models the ratio peaks in the range $0.03 \lesssim f_{eq} \lesssim 0.05$. At higher equilibrations the collisional ionization by electrons is increasingly effective, reducing the size of the neutral layer and reducing the broad to narrow ratio.

Although variations in f_{H^0} do affect the shape and position of the broad to narrow curves, the most conspicuous feature in Figure 10 is that the broad to narrow ratios are predominantly sensitive to f_{eq} (and hence v_S). The figure shows that the higher equilibration models match the observations best. In Hα, the predicted broad to narrow ratios fall slightly above the observed values. The best match occurs for full equilibration, where the model value lies $\sim$10% above the upper error bar of the observations. However, the Hβ broad to narrow ratio does agree with observations, favoring $f_{eq} \approx 0.8-1.0$ (T_e/T_p = 0.7−1.0 from Equation 10). Excluding the uncertainty in broad FWHM, the implied range of shock velocities is 300−365 km s^{-1}.

The disagreement between the observed and predicted Hα broad to narrow ratios may be due to the excitation cross sections utilized in the models. In the range of shock velocities implied by the observations, the thermal energy of the postshock electrons is $\lesssim$15 Rydbergs (1 Rydberg = 13.6 eV). At these energies, the collisional excitation cross sections are not as well determined as the cross sections at higher energies. This uncertainty is translated directly into the calculated broad to narrow ratios.

The Cygnus P7 shock lies $\sim 25'$ NW of the filament previously studied by RBFG83 and HRB94. In their analysis, HRB94 concluded that their observed shock has recently slowed due to an encounter with a density enhancement in the ISM. The shock observed by RBFG83 and HRB94 exhibits an Hα broad component width ~ 130 km s^{-1} and an Hα broad to narrow ratio ~ 1.6. In addition, faint [O III], [N II] and [S II] emission can be seen in this filament. These features are markedly different from those of Cygnus P7. In a pure Balmer line filament in the western Cygnus Loop, Treffers (1981) also measured an Hα broad component width ~ 130 km s^{-1}, with broad to narrow ratio ~ 1. Since the broad to narrow ratio is proportional to the ratio of the charge exchange rate to the ionization rate (CKR80, Smith *et al.* 1991), the difference between the Cygnus P7 broad to narrow ratio and those of other filaments may be due to the fact that the collisional ionization rate of hydrogen rises strongly with shock velocity for $100 \lesssim v_S \lesssim 300$ km s^{-1}. At a given equilibration, this would result in a decreasing broad to narrow ratio for this range of shock velocities.

Overall, our derived shock velocity for Cygnus P7 lies well above values obtained in most other optical studies of the Cygnus Loop. Previous observations using spectrophotometry (Raymond *et al.* 1980, RBFG83, Fesen, Kirshner & Blair 1982, Fesen & Itoh 1985, Raymond 1988, HRB94), Fabry Perot spectrometry (Kirshner & Taylor 1976, Treffers 1981, Shull & Hippelein 1991) and narrow band imagery (Fesen, Kwitter & Downes 1992, Levenson *et al.* 1998) have detected shock waves in various stages of evolution, from nonradiative to fully radiative. These observations have yielded shock velocities ~ 100 km s^{-1} for the bright, radiative filaments and $\sim 150-200$ km s^{-1} for the faint, partially radiative/nonradiative filaments. However, Kirshner & Taylor (1976) and Shull & Hippelein (1991) detected face-on Hα emission near the center of the Cygnus Loop, blueshifted to velocities $\sim 350-400$ km s^{-1}. These authors suggested that the face-on emission is produced by the supernova blast wave propagating into the low density ISM. Soft X-ray observations of the Cygnus Loop (Ku *et al.* 1984, Levenson *et al.* 1999) confirm the presence of fast (~ 400 km s^{-1}) shocks in this remnant, including locations where there is no optical emission (the preshock gas is fully ionized). The Cygnus P7 shock is similar in speed to both the X-ray determined blast wave velocity and the blueshifts seen by Kirshner & Taylor (1976) and Shull & Hippelein (1991).

Therefore, we conclude that the Balmer-dominated Cygnus P7 filament marks the current location of the supernova blast wave in the northeastern Cygnus Loop.

5.2. SW RCW 86

The Hα broad component width of the nonradiative shock RCW 86 SW (Figure 6) is 562±18 km s^{-1}, placing this shock at a Mach number intermediate between that of Cygnus P7 and Tycho Knot g. The narrow band Hα image (Figure 5) suggests that the shock geometry here is more complicated than for the Cygnus P7 shock, with multiple filaments surrounding the bright, clumpy emission covered by the slit. The forbidden line emission in the two-dimensional spectrum (Figure 5) indicates that part of the clumpy region has become radiative. Narrow band Hα and [S II] images of RCW 86 indicate that most of the bright clumpy emission seen in Figure 5 is produced by radiative shock waves (Smith 1997). From the one-dimensional spectrum in Figure 6 we estimate an Hα surface brightness of 4.2×10^{-5} ergs cm^{-2} s^{-1} sr^{-1} for the nonradiative shocks in SW RCW 86. This surface brightness is nearly twice that of Knot g (KWC87, Ghavamian 2000) and a factor of two or more brighter than the filament observed by HRB94. This property, along with the presence of radiative emission nearby, suggests an enhanced preshock neutral density in this part of the SNR. The velocity shift between the broad and narrow component centers in Figure 6 is smaller than the uncertainty in broad component width, indicating that the shock is viewed nearly edge-on.

Broad to narrow ratios were previously measured in RCW 86 by Long & Blair (1990), who obtained optical spectra of Balmer-dominated shocks in the N and SW (near our slit position). In SW RCW 86, they obtained an Hα broad component width of 600−780 km s^{-1} and a broad to narrow ratio of 0.65−0.94 for that line. These parameters are noticeably different from ours; the discrepancy is likely due to the fact that Long & Blair (1990) observed a partially radiative shock close to our slit position. This is evidenced by the faint [N II] and [S II] emission lines in their SW RCW 86 spectrum. In this case, slight contamination of the Hα narrow component by radiative Hα has likely lowered the broad to narrow ratio. In addition, the S/N in the Hα profile of RCW

86 SW is much lower in the Long & Blair (1990) data than ours, making their broad component line fit more uncertain.

We assembled a grid of shock models for equilibrations $f_{eq} = 0$, 0.03, 0.05, 0.2, 0.5, 0.8 and 1.0. These equilibrations yield the observed FWHM for shock velocities of 565, 570, 573, 575, 634, 710 and 775 km s^{-1}, respectively. The predicted broad to narrow ratios appear in Figure 11, computed for the case $n_0 = 1$ cm^{-3}. As with Cygnus P7, models with higher equilibration match the observations somewhat better than the low equilibration models. From Figure 11, $f_{eq} \approx 0.4-0.5$ ($T_e/T_p \approx 0.25-0.33$) simultaneously matches the Hα and Hβ broad to narrow ratios. The implied shock velocity is 600−635 km s^{-1}.

The ability to simultaneously determine both the velocity and equilibration of Balmer-dominated shocks is a potentially useful aid in modeling the X-ray emission from SNRs. The ASCA study of RCW 86 by Borkowski *et al.* (2000) is one particular example. The Balmer-dominated shocks in SW RCW 86 lie close to one of the ASCA spectral extraction windows used by Borkowski *et al.* (2000). In this section of the remnant, the X-ray emission is dominated by nonthermal continuum from fast ($v_S \sim 600-1000$ km s^{-1}) shocks, with thermal emission lines barely detected. Borkowski *et al.* (2000) noted that the portion of SW RCW 86 lying in the ASCA window features a variety of shock speeds and that characterizing the thermal and nonthermal emission requires a large number of free parameters. This makes the X-ray modeling of SW RCW 86 quite difficult. We note that in the future, velocities and equilibrations predicted by our Balmer-dominated shock models may be used to reduce the number of free parameters needed to model the X-ray data of RCW 86 (and other SNRs).

5.3. Tycho Knot g

We compared data from Knot g (1) with shock model predictions for equilibrations of 0, 0.03, 0.05, 0.2, 0.5, 0.8 and 1.0, corresponding to shock velocities of 2050, 2075, 2090, 2175, 2375, 2635 and 2900 km s^{-1}. We allowed the preshock neutral fraction to vary from 0.99 to 0.1. We

present the predicted broad to narrow ratios for Knot g (1) in Figure 12. The models are unable to match the observed Hα broad to narrow ratio, although the Hβ broad to narrow ratio is consistent with $f_{eq} \lesssim 0.2$ ($T_e/T_p \lesssim 0.1$). This is similar to the limit on T_e/T_p derived by Laming *et al.* (1996) for a shock of similar speed in SN 1006. Ignoring the measurement uncertainty in broad component width, the corresponding shock velocity of Knot g (1) is 2050−2175 km s^{-1}. The minimum in I_b/I_n occurs for an equilibration of 3%−5%; this corresponds to the optimum electron temperature for Balmer line excitation in the narrow component (the opposite of what occurs in the slower shock models). Models with high preshock neutral fractions ($\gtrsim 0.8$) match the Hβ broad to narrow ratio best; this result agrees with predictions of our photoionization precursor models (Ghavamian *et al.* 2000). The high neutral fraction may be explained by the H I 21 cm observations of Reynoso *et al.* (1999), which suggest that the eastern edge of Tycho is encountering a warm H I cloud. On the other hand, X-ray observations (Hwang, Hughes & Petre 1998, Seward 1983) and evolutionary models (Dwarkadas & Chevalier 1997) of Tycho's SNR indicate a total preshock density $\lesssim 1.1$ cm^{-3}. Taken together, the optical, X-ray and radio data suggest that Knot g is probably encountering the extreme (low density) edge of the H I cloud.

6. Discussion

One obvious problem is the failure of the models to reproduce the observed Hα broad to narrow ratio for Tycho Knot g (1). The predicted Hβ broad to narrow ratios do agree with the observations, although this is due in part to the larger error bars. Taking $A_V = 1.6$, the predicted narrow component Balmer decrement falls below the observed value, regardless of the equilibration or Lyman line trapping efficiency. The disagreement between the observed and predicted broad to narrow ratios may be partly due to the proton excitation cross sections utilized by the shock code. The proton cross sections are most uncertain at low energy,~ 10 keV. Since the proton thermal energy in the Knot g (1) shock lies close to this value, the Hα and Hβ excitation rates computed from these cross sections (including charge transfer into excited states) will be correspondingly uncertain. This situation is similar to the problem mentioned earlier with the Cygnus P7 models,

where the uncertain quantity was the electron excitation cross section near threshold.

An alternate explanation of the discrepant Hα broad to narrow ratio is collisional excitation of H in a spatially unresolved precursor. If the upstream H is collisionally excited before entering the Knot g shock, the resulting Hα and Hβ emission will add to the overall narrow component flux from the shock. In an earlier paper (Ghavamian *et al.* 2000) we presented a high resolution Hα spectrum which indicated that the neutrals are heated to a temperature $\sim$40,000 K just before entering the shock. At temperatures $\sim 10^4$ K, collisional excitation produces an optical spectrum with a steep Balmer decrement; this could explain why the narrow component Hα flux is so enhanced relative to that of Hβ. The Balmer-dominated spectrum of Tycho would then result from the superposition of precursor + postshock neutral excitation.

It would be appropriate here to speculate on the relationship between f_{eq} and the magnetosonic Mach number M_S ($= v_S/(c_S^2 + v_A^2)^{1/2}$, where c_S is the sound speed and v_S is the Alfvén speed in the preshock gas). There is a clear trend of decreasing equilibration with higher M_S (see Table 5). Cargill & Papadapoulos (1988) have argued that for low Mach number shocks propagating perpendicular to the interstellar magnetic field, a series of plasma instabilities are initiated by the protons just behind the shock. As the protons gyrate about the field lines, some of them re-enter the upstream region, counterstreaming into the preshock gas. Laming (1998, 2001) and Bingham *et al.* (1997) have pointed out that if the reflected protons follow a beamlike (monoenergetic) distribution, a two-stream instability will develop. Lower hybrid waves generated by the instability can be in resonance with protons and electrons simultaneously, allowing energy transfer between the two particle species. A key difference between perpendicular shocks with $M_S \sim 20-50$ (like Cygnus P7 and SW RCW 86) and those with $M_S \sim 200$ like those in Tycho) is that the former are expected to be laminar (i.e., steady) while the latter are expected to be highly turbulent (Tidman & Krall 1971). Due to the unsteady nature of high Mach number shocks, reflected protons are likely to exhibit an angular spread in velocities, inhibiting the growth of the two-stream instability and reducing the efficiency of electron heating. Electron heating by lower hybrid waves has been used to explain X-ray emission from comet C/Hyakutake (Bingham *et al.* 1997), the nonthermal

X-ray tail observed in Cas A spectra (Laming 2001) and the injection of thermal particles into the cosmic ray acceleration process (McClements *et al.* 1997).

There is strong evidence of an inverse relation between f_{eq} and M_S from spacecraft observations of solar wind shocks. Schwartz *et al.* (1988) presented ISEE data from 14 interplanetary shocks, as well as 66 crossings of the Earth's bow shock. They found that across the shock transition electrons are heated relative to the protons by an amount which scales as $1/M_S$. Interestingly, the fractional equilibrations we derive from our analysis follow roughly the same trend. The shocks studied by Schwartz *et al.* only reach $M_S \sim 20$, while our observations cover $25 \lesssim M_S \lesssim 200$. The equilibration fraction determined by Laming *et al.* (1996) for a nonradiative shock in SN 1006 agrees with the value found simply by extrapolating $f_{eq} \propto 1/M_S$ from the lower Mach number shocks of Schwartz *et al.* (1988) to the values found in SN 1006 ($M_S \sim 250$).

It is interesting to note that according to the results of Cargill & Papadapoulos (1988), collisionless heating proceeds more efficiently for shocks propagating perpendicular to the interstellar magnetic field. There may be a connection between the more efficient equilibration predicted for perpendicular shocks and the limb brightening seen in radio observations of barrel shaped remnants. In these cases, the limb brightening occurs in parts of the remnant which propagate perpendicular to the magnetic field (Gaensler 1998). The radio (and sometimes X-ray) emission from these remnants is synchrotron radiation from electrons energized by first order Fermi acceleration, a process where electrons are boosted to relativistic energies by scattering back and forth between upstream and downstream turbulence (Jones & Ellison 1991, Reynolds & Gilmore 1986, Blandford & Eichler 1987, Jones & Ellison 1991). Fulbright & Reynolds (1990) proposed that the enhanced radio emission occurs because the Fermi acceleration process is more efficient for perpendicular shocks. From the work of McClements *et al.* (1997) and Laming (1998), it appears that the same plasma instabilities which heat the electrons in strong shocks can also inject particles into the cosmic ray acceleration process. Clearly, the relationship between magnetic field orientation, equilibration and cosmic ray acceleration deserves a more detailed investigation.

7. Conclusions

To investigate the properties of nonradiative shocks, we have obtained high S/N spectra of the Cygnus Loop, RCW 86 and Tycho covering a factor of 10 in Mach number. In each remnant, we have measured broad to narrow ratios of both Hα and Hβ. We find that the broad to narrow ratios show considerable variation from one remnant to the next, with the Hβ ratio systematically larger than that of Hα. The difference between the two ratios is evidence of Lyman line trapping in the narrow component.

We have devised a numerical code which predicts the ionization structure behind a nonradiative shock and uses a Monte Carlo simulation to calculate the influence of Ly β and Ly γ trapping on the Hα and Hβ emission lines. We have modeled the Hα and Hβ broad to narrow ratios in three of the observed shocks: Cygnus P7 (v_S = 300−400 km s^{-1}), SW RCW 86 (v_S = 580−660 km s^{-1}) and Tycho Knot g (v_S = 1940−2300 km s^{-1}). Overall, the shock code matches the observations in the first two remnants, but yields only marginal agreement for Tycho Knot g. The models indicate nearly complete equilibration for Cygnus P7 and half equilibration for RCW 86 SW, evidence for substantial collisionless heating in these nonradiative shocks. In Knot g, the predicted Hα broad to narrow ratios are systematically larger than the observed values for all equilibrations. The difficulty in modeling the Knot g broad to narrow ratio may be due to the large uncertainty in proton excitation cross sections near threshold. However, the models do successfully reproduce the observed Hβ broad to narrow ratios. From the Hβ results, we infer a low equilibration for Tycho, $\lesssim 20\%$. This value is consistent with the findings of Laming *et al.* (1996), who used ultraviolet observations with HUT to determine the equilibration of shocks of similar strength in SN 1006.

For a given shock velocity, we find that the thickness of the ionization layer depends on the electron-proton temperature equilibration. At shock velocities $\lesssim 1000$ km s^{-1}, the collisional ionization of hydrogen is dominated by the electrons; the greater the equilibration, the thinner the ionization layer. This trend is reversed at high shock velocities. Above 2500 km s^{-1}, proton ionization dominates electron ionization; therefore the more equilibrated the shock, the thicker the

ionization layer.

P. G. would like to the thank J. Weisheit, J. M. Laming and R. Bandiera for several helpful discussions. We would also like to thank the anonymous referee for valuable suggestions in improving the presentation of this paper. The work of P. G. was supported by grant D70832 from Rice University, STScI grant GO-07515-02.96A, NSF atomic physics theory grant PHY-9772634 and student travel support from CTIO. P.G. also acknowledges the hospitality of the Harvard-Smithsonian Center for Astrophysics, where some of this paper was completed. The work of J. R. was supported by NASA grant NAG 5-2845.

REFERENCES

Aldcroft, T. L., Romani, R. W. & Cordes, J. M. 1992, ApJ 400, 638

Bandiera, R. 1998, private communication

Bingham, R., Dawson, J. M., Shapiro, V. D., Mendis, D. A. & Kellett, B. J. 1997, Science 275, 49

Blair, W. P., Long, K. S. & Vancura, O. 1991, ApJ 366, 484

Borkowski, K. J., Rho, J., Reynolds, S. P. & Dyer, K. K. 2000, ApJ, submitted

Cargill, P. J. & Papadapoulos, K. 1988, ApJ 329, L29

Chevalier, R. A. & Raymond, J. C. 1978, ApJ 225, L27

Chevalier, R. A., Kirshner, R. P. & Raymond, J. C. 1980, ApJ 235, 186 (CKR80)

Draine, B. T. & McKee, C. F. 1993, ARA&A 31

Dwarkadas, V. V. & Chevalier, R. A. 1998, ApJ 497, 807

Feldman, W. C., Asbridge, J. R., Bame, S. J., Gosling, J. T. & Zwickl, R. D. 1983, in *Solar Wind Five*, NASA Conf. Publ., CP-2280

Fesen, R. A., Blair, W. P. & Kirshner, R. P. 1982, ApJ 262, 171

Fesen, R. A. & Itoh, H. 1985, ApJ 295, 43

Fesen, R. A., Kwitter, K. B. & Downes, R. A. 1992, AJ 104, 719

Freeman, E. L. & Jones, E. M 1974, *Atomic Collision Processes in Plasma Physics Experiments I*, UKAEA Report No. CLM-R137 Culham Laboratory: Abingdon, England

Fulbright, M. S. & Reynolds, S. P. 1990, ApJ 357, 591

Gaensler, B. M. 1998, ApJ 493, 781

Ghavamian, P. 1999, PhD thesis, Rice University

Ghavamian, P., Raymond, J., Blair, W. P. & Hartigan, P. 2000, ApJ535, in press

Giovanardi, C., Natta, A. & Palla, F. 1987, A&AS 70, 269

Hesser, J. E. & van den Bergh, S. 1981, ApJ 251, 549

Hester, J. J., Raymond, J. C. & Blair, W. P. 1994, ApJ 420, 721 (HRB94)

Hwang, U., Hughes. J. P. & Petre, R. 1998, ApJ 497, 833

Janev, R. K., Langer, W. D., Evans, K., Jr. & Post, D. E. Jr. 1987, *Elementary Processes in Hydrogen-Helium Plasmas*, New York: Springer Verlag

Kaastra, J. S., Asaoka, I., Koyama, K. & Yamauchi, S. 1992, A&A 264, 654

Kamper, K. & van den Bergh, S. 1978, ApJ 224, 851

Kirshner, R. P., Winkler, P. F. & Chevalier, R. A. 1987, ApJ 315, L135 (KWC80)

Ku, W. H.-M., Kahn, S. M., Pisarski, R. & Long, K. S. 1984, ApJ 278, 615

Laming, J. M., Raymond, J. C., McLaughlin, B. M. & Blair, W. P. 1996, ApJ 472, 267

Laming, J. M. 1998, ApJ 499, 309

Laming, J. M. 2001, ApJ 546, in press

Leibowitz, E. M. & Danziger, J. J. 1983, MNRAS 204, 273

Levenson, N. A., Graham, J. R., Keller, L. D. & Richter, M. 1998, ApJS 118, 541

Levenson, N. A., Graham, J. R. & Snowden, S. L. 1999, ApJ 526, 874

Long, K. S., Blair, W. P. & van den Bergh, S. 1988, ApJ 333, 749

Long, K. S. & Blair, W. P. 1990, ApJ 358, L13

Martín, F. 1999, Journal of Physics B 32, 501

McClements, K. G., Dendy, R. O, Bingham, R., Kirk, J. G. & Drury, L. O'C. 1997, MNRAS 291, 241

McLaughlin, B. M., Winter, T. G. & McCann, J. F. 1998, Journal of Physics B 30, 1043

Petruk, O. 1999, A&A 346, 961

Raymond, J. C., Davis, M., Gull, T. R. & Parker, R. A. R. 1986, ApJ 238, L21

Raymond, J. C., Blair, W. P., Fesen, R. A. & Gull, T. R. 1983, ApJ 275, 636 (RBFG83)

Raymond, J. C., Hester, J. J., Cox, D. P., Blair, W. P., Fesen, R. A. & Gull, T. R. 1988, ApJ 324, 869

Rosado, M., Ambrocio-Cruz, P., Le Coarer, E. & Marcelin, P. F. 1991, Rev. Mex. Astron. Astrof. 315, 243

Schwartz, S. J., Thomsen, M. F., Bame, S. J. & Stansberry, J. 1988, JGR 93, 12923

Schweizer, F. & Lasker, B. M. 1978, ApJ 226, 167

Seward, F., Gorenstein, P. & Tucker, W. 1983, ApJ 266, 287

Shah, M. B. & Gilbody, H. B. 1981, Journal of Physics B 14, 2361

Shah, M. B., Elliott, D. S. & Gilbody, H. B. 1987, Journal of Physics B 20, 2481

Shah, M. B., Geddes, J., McLaughlin, B. M. & Gilbody, H. B. 1998, Journal of Physics B 31, L757

Shull, P. & Hippelein, H. 1991, ApJ 383, 714

Smith, R. C., Kirshner, R. P., Blair, W. P. & Winkler, P. F. 1991, ApJ 375, 652

Smith, R. C., Raymond. J. C. & Laming, J. M. 1994, ApJ 420, 286

Smith, R. C. 1997, AJ 114, 2664

Spitzer, L. Jr. 1940, MNRAS 100, 396

Spitzer, L. Jr. 1962, *Physics of Fully Ionized Gases*, New York: Wiley

Tidman, D. A. & Krall, N. A. 1971, *Shock Waves in Collisionless Plasmas*, New York: Wiley

Treffers, R. R. 1981, ApJ 250, 213

Truelove, J. K. & McKee, C. F. 1999, ApJS 120, 299

Tuohy, I. R., Dopita, M. A., Mathewson, D. S., Long, K. S. & Helfand, D. J. 1982, ApJ 261, 473

Vink, J., Kaastra, J. S. & Bleeker, A. M. 1997, A&A 328, 628

Weisheit, J. 1998, private communication

Whelan, C. T. 1986, Journal of Physics B 19, 2355

Winkler, P. F. & Long, K. S. 1997, ApJ 491, 829

This manuscript was prepared with the AAS LaTeX macros v4.0.

Fig. 1.— Top: Red image from the Palomar Optical Sky Survey, showing the P7 nonradiative shock in NE Cygnus Loop. The approximate position and width of the FAST spectrograph slit is marked. Bottom: Two-dimensional sky subtracted spectrum of position P7, showing the Hα broad and narrow components. Extraction aperture for the one-dimensional spectrum is indicated by a bracket. East is at the top.

Fig. 2.— The extracted one-dimensional Hα and Hβ profiles of Cygnus Loop P7.

Fig. 3.— Top: Narrow band Hα image of Tycho, acquired with the direct imager at the 4m telescope at KPNO. The FAST slit position is indicated. Bottom: The two-dimensional sky subtracted spectrum of Knot g, showing broad and narrow Hα emission. The broad component is lost in the noise near the bottom of the slit, where the emission is faintest. Extraction aperture for the one-dimensional spectrum (position 1 in the text) is indicated by a bracket. North is at the top.

Fig. 4.— The one-dimensional Hα and Hβ profiles of Knot g (1). The spectrum has not been corrected for interstellar reddening.

Fig. 5.— Top: the southwestern portion of RCW 86, from Smith (1997). The Balmer-dominated filaments covered by the slit are among the brightest nonradiative shocks observed to date. Radiative emission can be seen in the upper right side of the image. Bottom: the two-dimensional sky subtracted spectrum of the southwestern filament. The extraction aperture of the one-dimensional spectrum is indicated by a bracket. Northwest is located at the top.

Fig. 6.— Hα and Hβ line profiles for southwest RCW 86. No reddening correction has been applied.

Fig. 7.— The electron and proton temperatures predicted by the jump conditions, shown for a range of shock velocities and equilibrations. The calculation assumes a pure H gas.

Fig. 8.— Ionization structures of four nonradiative shocks, shown for a 50% preionized medium with total number density of 1 cm^{-3}. Densities of fast and slow neutrals are plotted vs. postshock distance for the cases of no equilibration ($f_{eq} = 0$) and full equilibration ($f_{eq} = 1$) at the shock front.

Fig. 9.— The variation of broad component FWHM with shock velocity, computed for different equilibrations using Equation 11. The numerical values in the figure have been computed for a nonradiative shock viewed edge-on.

Fig. 10.— The predicted broad to narrow ratios for Cygnus Loop P7 (broad FWHM = 262±32 $\mathrm{km\,s^{-1}}$), shown vs. equilibration fraction f_{eq} for three different preshock neutral fractions (n_0 = 1 $\mathrm{cm^{-3}}$). Each equilibration combines with a unique shock velocity to yield the observed broad FWHM. Horizontal dashed lines mark the range of broad to narrow ratios derived from observations.

Fig. 11.— The predicted broad to narrow ratios for RCW 86 SW (2) (broad FWHM = 562±18 $\mathrm{km\,s^{-1}}$), shown vs. equilibration fraction f_{eq} for three different preshock neutral fractions (n_0 = 1 $\mathrm{cm^{-3}}$). Each equilibration combines with a unique shock velocity to yield the observed broad FWHM. Horizontal dashed lines mark the range of broad to narrow ratios derived from observations.

Fig. 12.— The predicted broad to narrow ratios for Tycho Knot g (1) (broad FWHM = 1765±118 $\mathrm{km\,s^{-1}}$), shown vs. equilibration fraction f_{eq} for three different preshock neutral fractions (n_0 = 1 $\mathrm{cm^{-3}}$). Each equilibration combines with a unique shock velocity to yield the observed broad FWHM. Horizontal dashed lines mark the range of broad to narrow ratios derived from observations.

Table 1. Journal of Spectroscopic Observations

Target	α(2000)	δ(2000)	Date (UT)	Range (Å)	P.A.[a]	Exposure (s)
Cygnus P7	20:54:32.5	32:17:32.8	1997 Oct 7	6050-7050	90°	6×900
Cygnus P7	20:54:32.5	32:17:32.8	1998 Sep 26	4370-5370	90°	11×1800
RCW 86 SW	14:41:08.1	−62:43:54.5	1998 Apr 6	5800-7430	128.7°	4×900
RCW 86 SW	14:41:08.1	−62:43:54.5	1998 Apr 8	4610-5110	128.7°	3×1800
Tycho Knot g	00:25:50.9	64:09:19.2	1997 Oct 10	3600-7600	−10°	6×1800

[a]Measured E of N

Table 2. Present and Prior Hα Measurements of the Knot g Broad Component

Paper	FWHM ($\mathrm{km\,s^{-1}}$)	ΔV_{bn} ($\mathrm{km\,s^{-1}}$)[a]	I_b/I_n
Chevalier, Kirshner & Raymond (1980)	1800±200	···	0.4−1.3
Kirshner, Winkler & Chevalier (1987)	1800±100	238±18	1.08±0.16
Smith *et al.* (1991)	1900±300	240±60	0.77±0.09
Present Work: Knot g (1)	1765±110	132±35	0.67±0.1[b]
Present Work: Knot g (2)	2105±130	< 130	0.75±0.1[b]

[a]Velocity shift between broad component line center and narrow component

[b]Broad to narrow ratio corrected for contribution from diffuse emission

Table 3. Tycho Knot g (1) Balmer Decrements

A_V[a]	Hα/Hβ (broad)	Hα/Hβ (narrow)	Hα/Hβ (total)
Undereddened	$6.11^{+8.0}_{-2.51}$	$9.93^{+1.57}_{-1.23}$	$7.97^{+4.47}_{-2.27}$
1.6	$3.67^{+4.83}_{-1.5}$	$5.96^{+0.93}_{-0.73}$	$4.78^{+2.7}_{-1.36}$
2.6	$2.66^{+3.52}_{-1.08}$	$4.33^{+0.68}_{-0.53}$	$3.48^{+1.95}_{-0.99}$

[a]A_V = 1.6 and 2.6 correspond to the range of visual extinction parameters inferred for Tycho (Chevalier, Kirshner & Raymond 1980).

Table 4. Line Profile Fits

Target	I_b/I_n (Hα)	I_b/I_n (Hβ)	Broad FWHM (km/s)	v_S (km/s)[a]
Cygnus P7	0.59±0.3	0.99±0.3	262±32	235−395
RCW 86 SW	1.18±0.03	1.54±0.17	562±18	545−793
Tycho Knot g	0.67±0.1[b]	1.15±0.3	1765±110	1940−3010

[a]Extrema in shock velocity v_S correspond to the equilibrated and unequilibrated cases, respectively. Quoted v_S includes uncertainty in broad FWHM.

[b]Corrected for contribution from diffuse emission.

Table 5. Shock Parameters Predicted by Numerical Models

Shock	f_{eq}	T_e/T_p	v_S (km s^{-1})[a]
Cygnus P7	0.8−1.0	0.67−1.0	300−400
SW RCW 86	0.4−0.5	0.25−0.33	580−660
Tycho Knot g (1)	≤ 0.2	≤ 0.1	1940−2300

[a]Includes measurement uncertainty of broad component width.

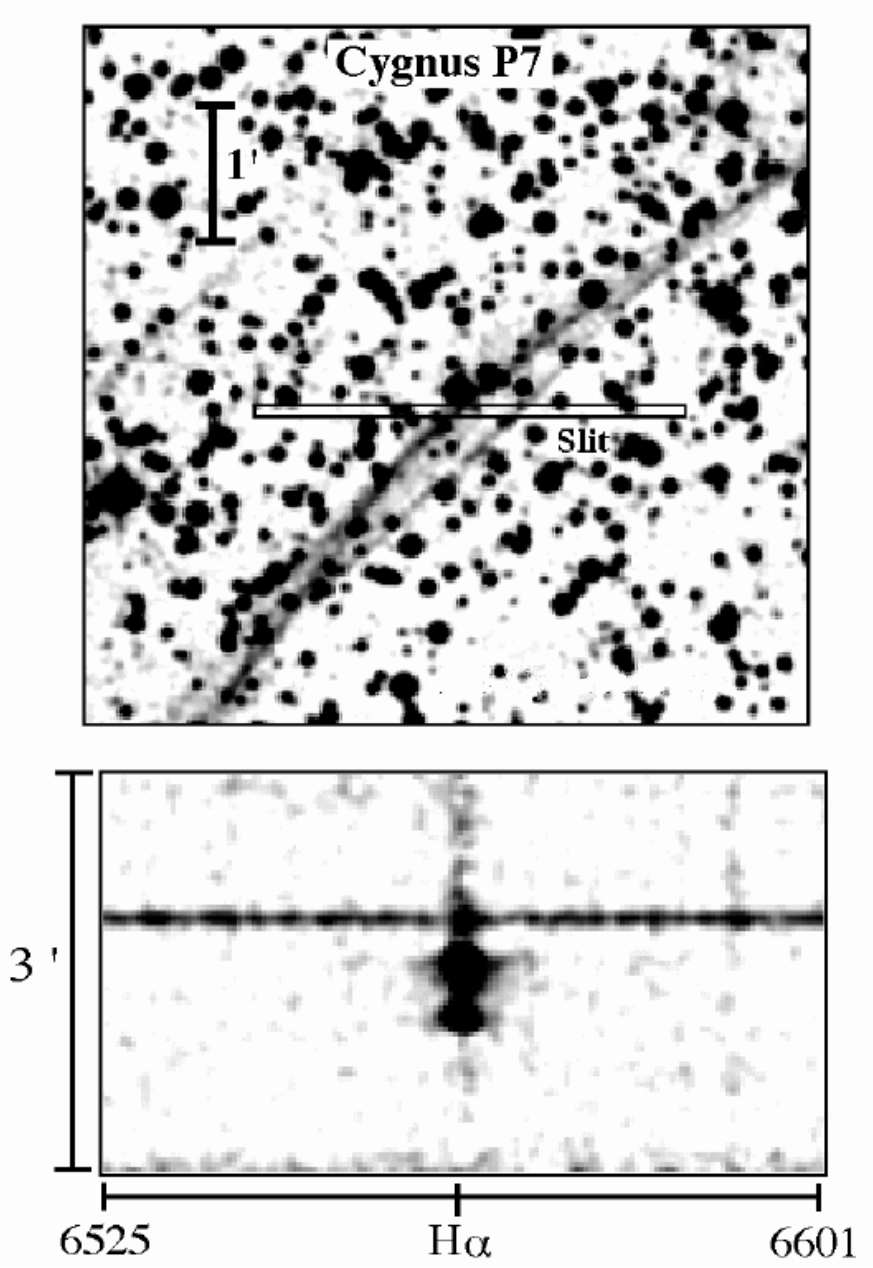
Cygnus P7
1'
Slit
3 '
6525
Hα
6601

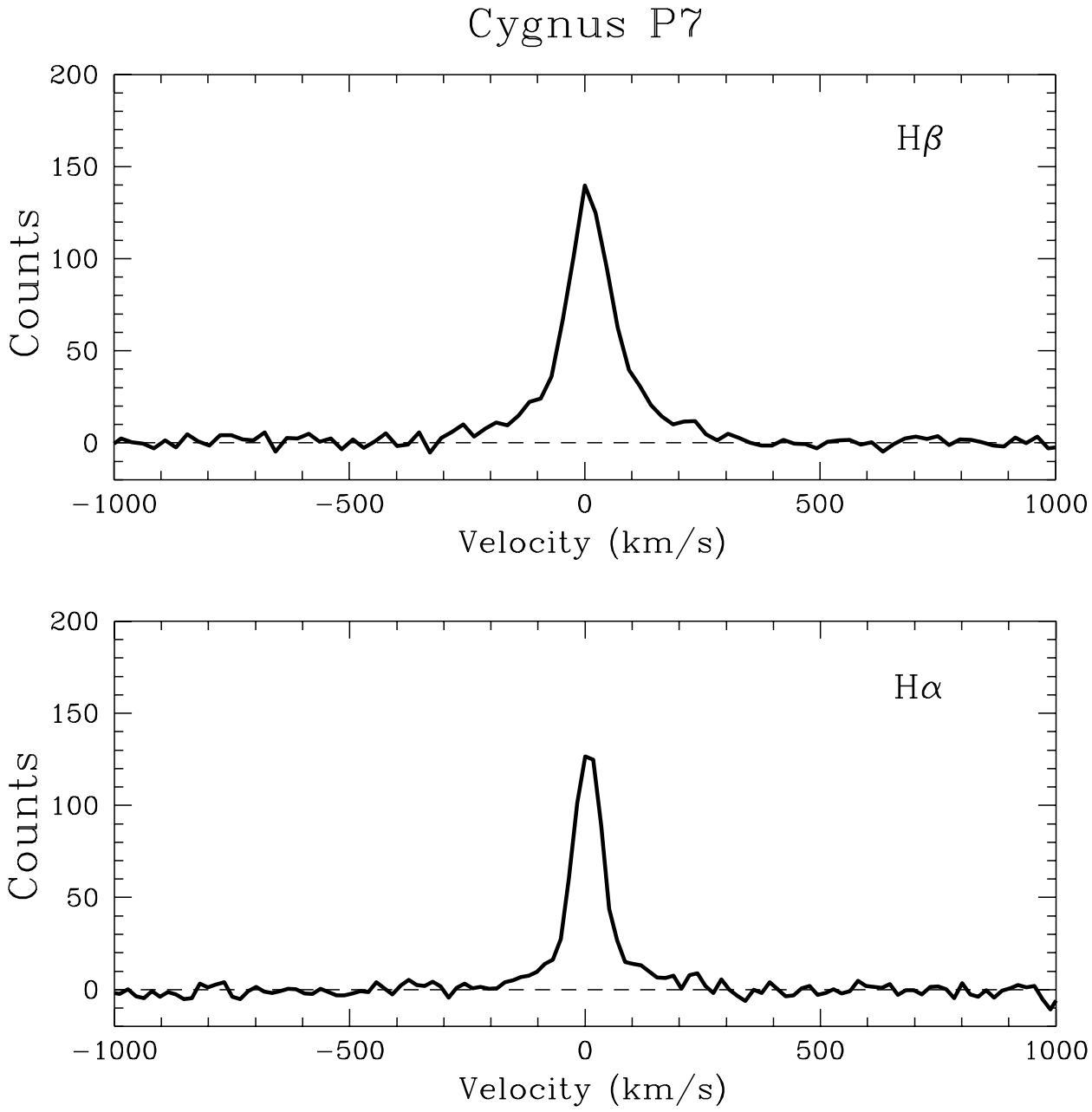
Cygnus P7
Hβ
Hα
Counts
Velocity (km/s)
200
150
100
50
0
−1000
−500
0
500
1000

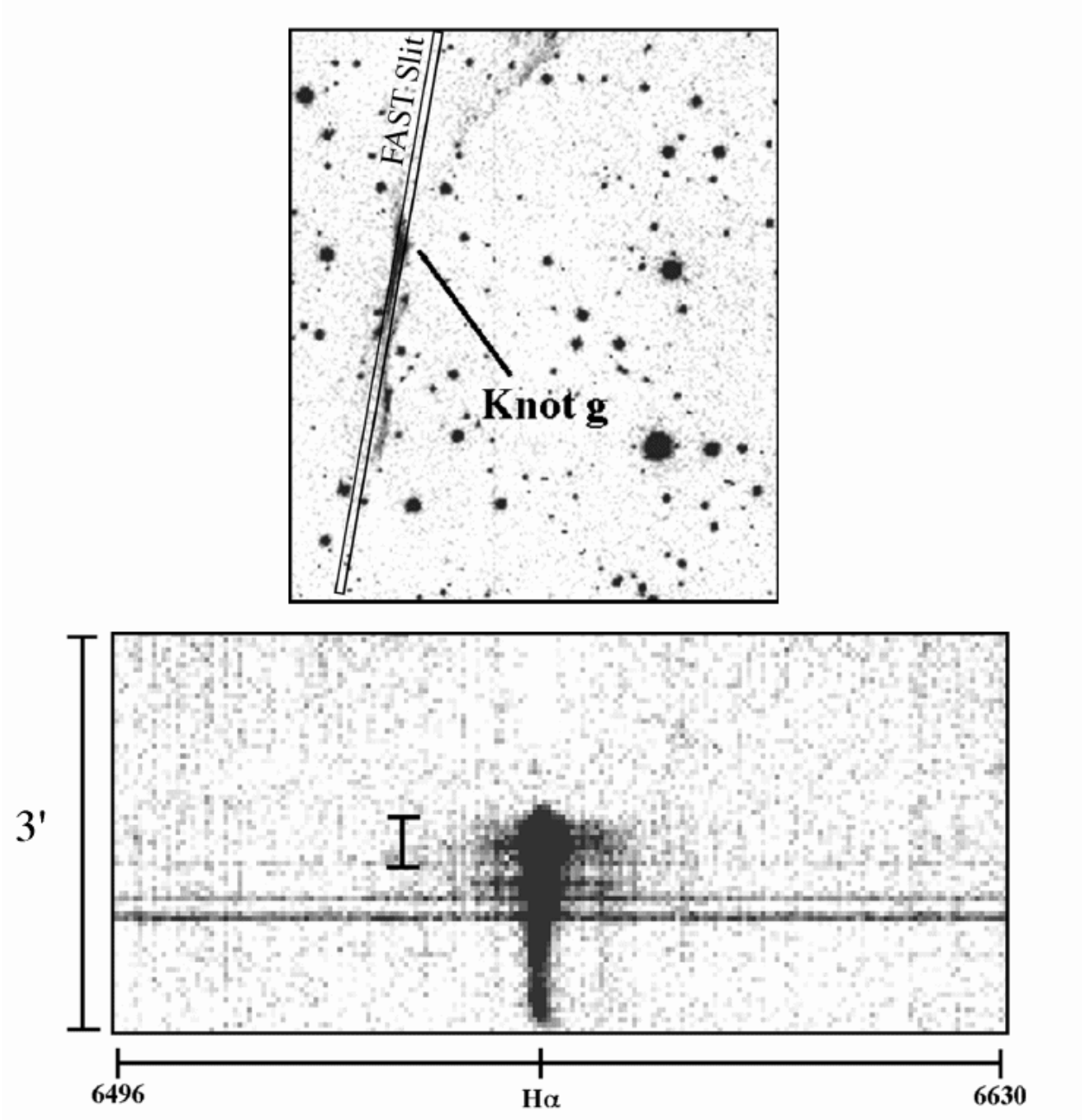
FAST Slit
Knot g
3'
6496
Hα
6630

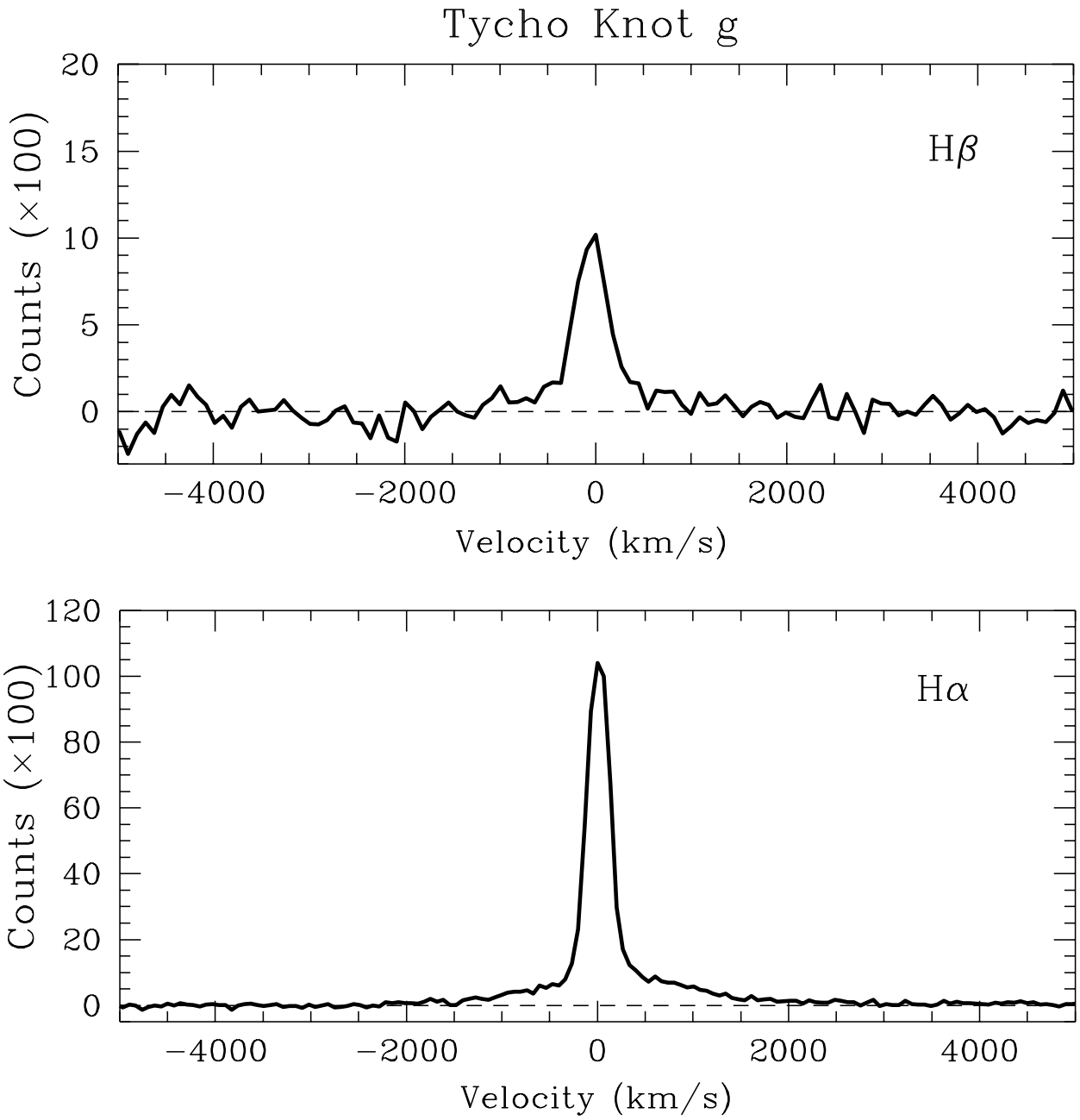
Tycho Knot g
Hβ
Counts (×100)
Velocity (km/s)
Hα
Counts (×100)
Velocity (km/s)

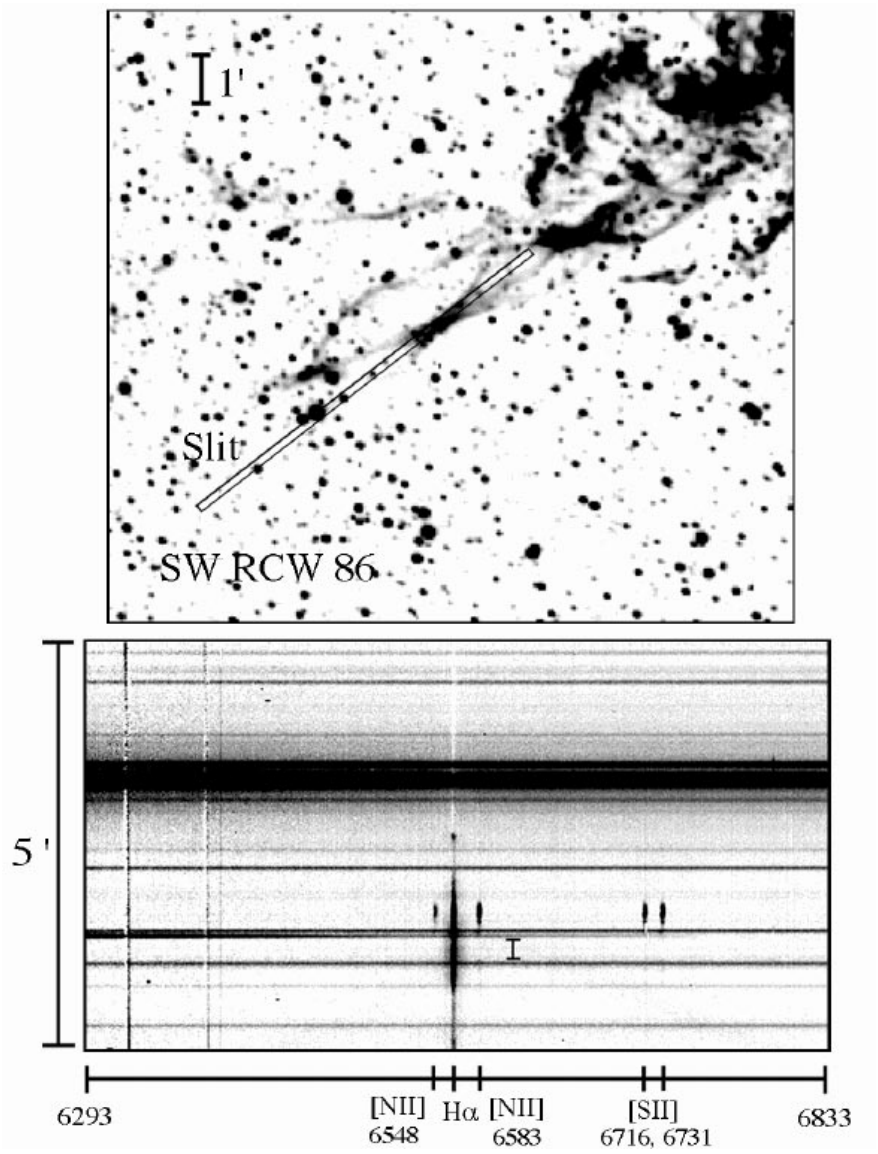
1'
Slit
SW RCW 86
5 '
6293
[NII]
6548
Hα
[NII]
6583
[SII]
6716, 6731
6833

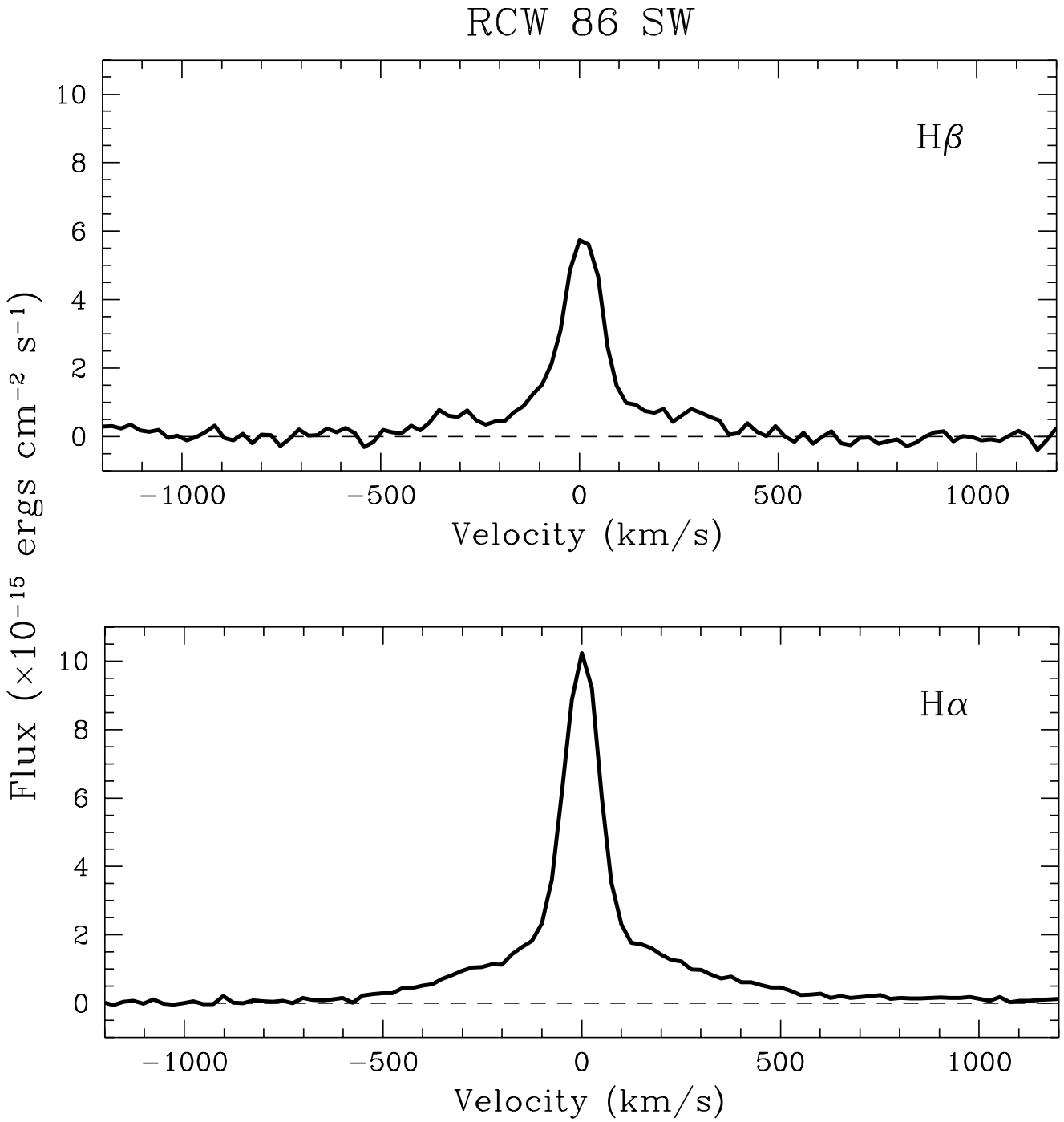
RCW 86 SW
Hβ
Hα
Flux (×10⁻¹⁵ ergs cm⁻² s⁻¹)
Velocity (km/s)
Velocity (km/s)
0
2
4
6
8
10
−1000
−500
0
500
1000

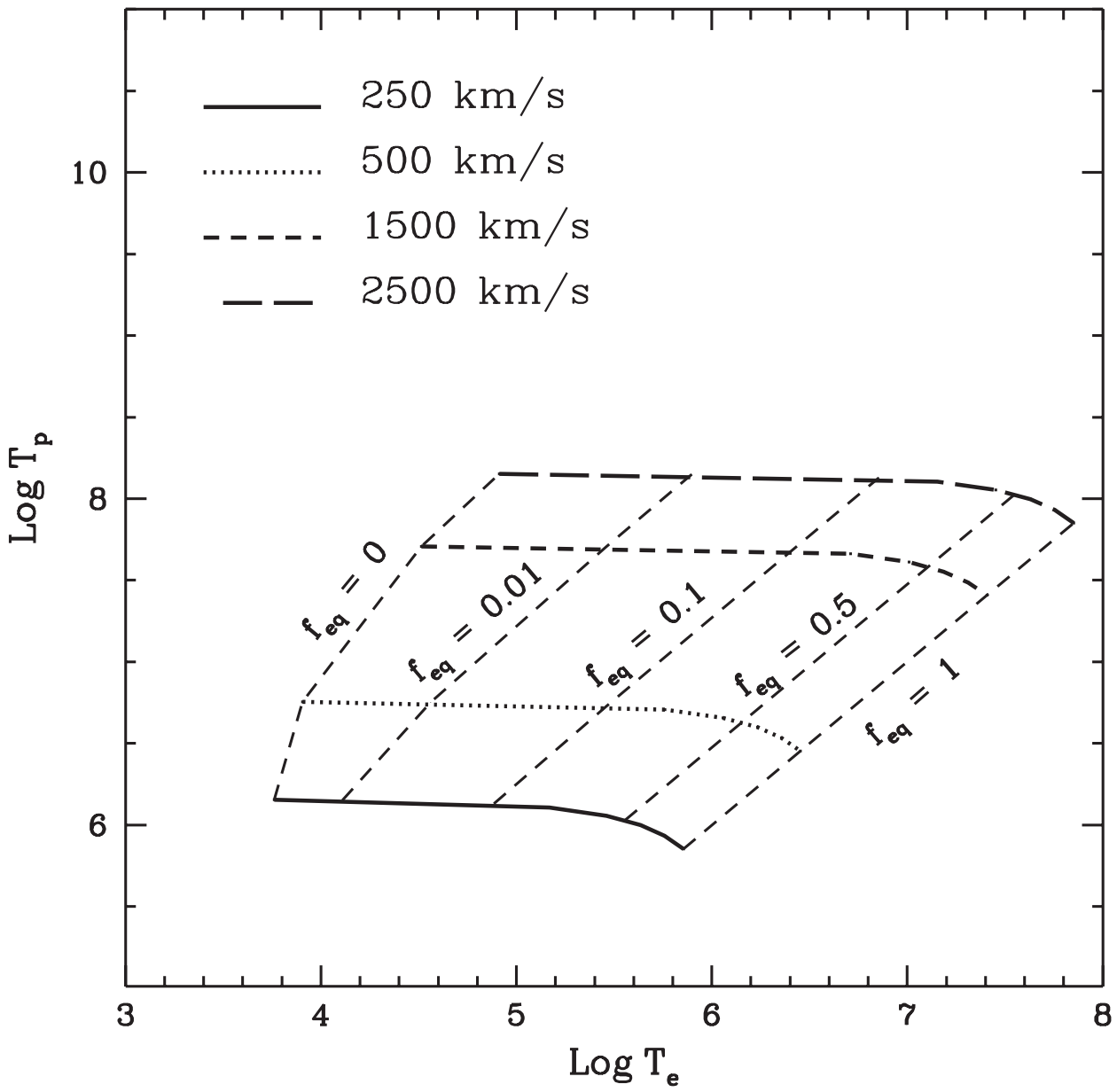
250 km/s
500 km/s
1500 km/s
2500 km/s
f_{eq} = 0
f_{eq} = 0.01
f_{eq} = 0.1
f_{eq} = 0.5
f_{eq} = 1
Log T_p
Log T_e
10
8
6
3
4
5
6
7
8

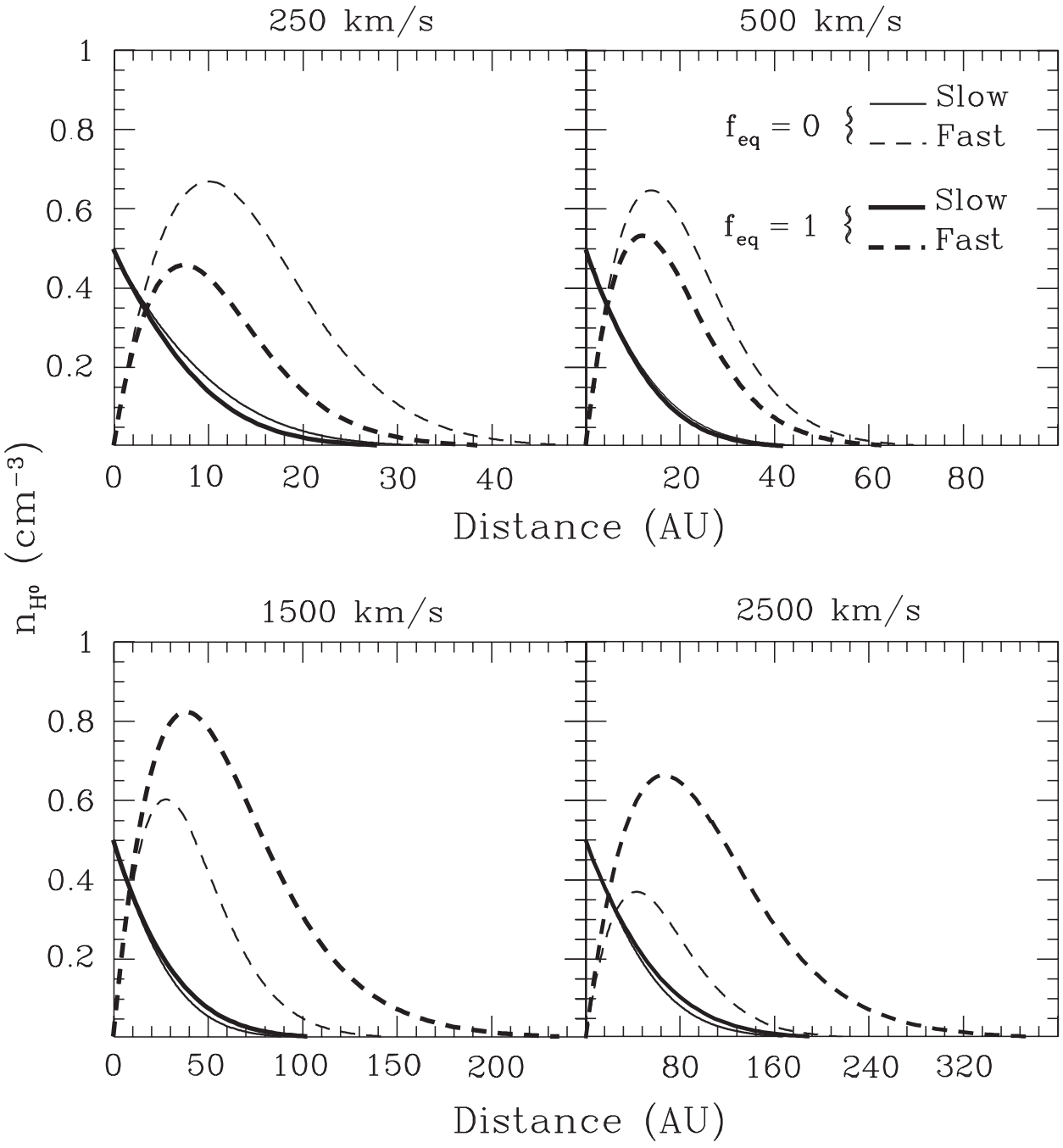
250 km/s
500 km/s
1500 km/s
2500 km/s
n_{H^0} (cm^{-3})
Distance (AU)
Distance (AU)
f_{eq} = 0
Slow
Fast
f_{eq} = 1
Slow
Fast

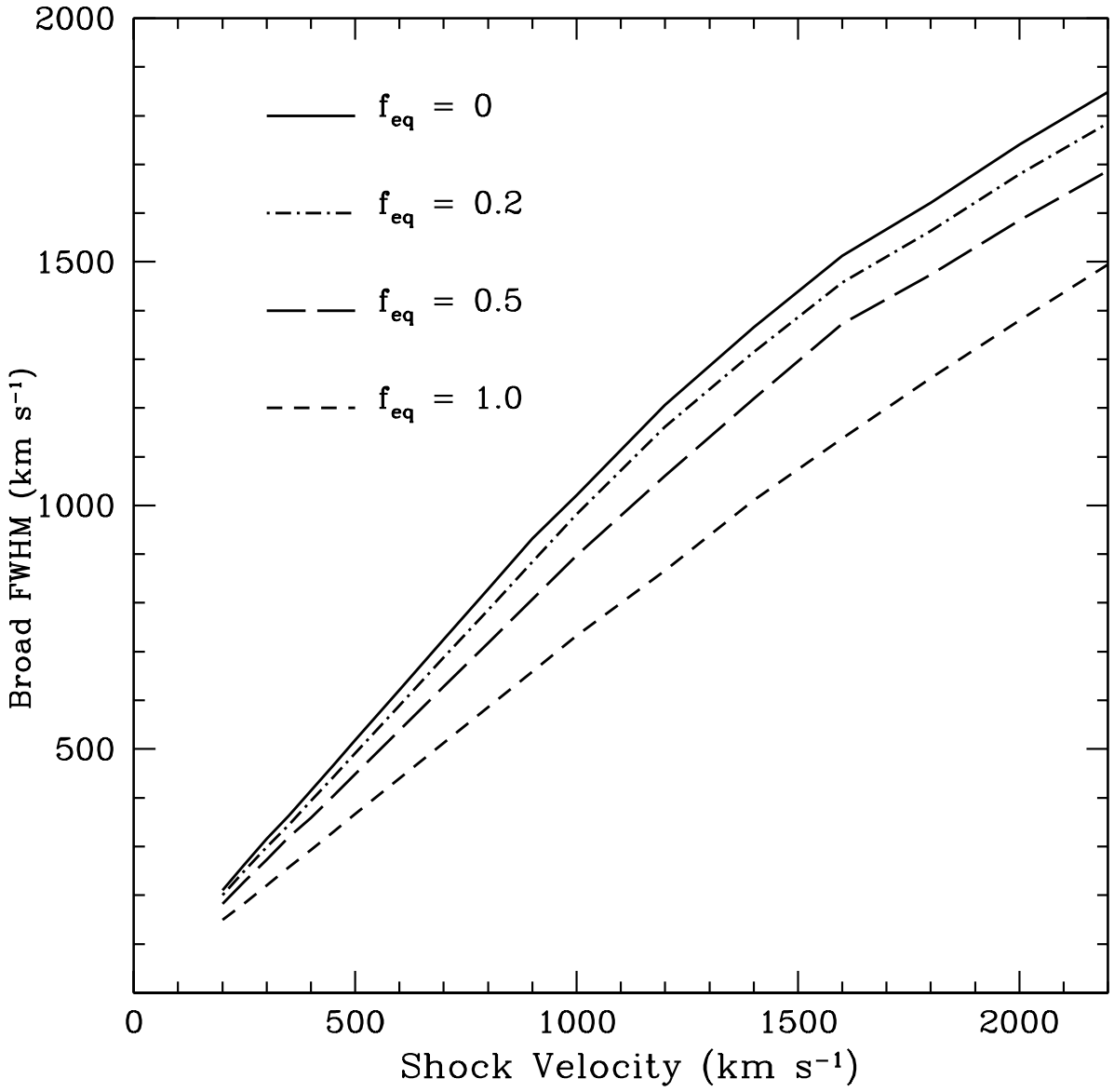
2000
1500
1000
500
0
500
1000
1500
2000
Broad FWHM (km s⁻¹)
Shock Velocity (km s⁻¹)
f_eq = 0
f_eq = 0.2
f_eq = 0.5
f_eq = 1.0

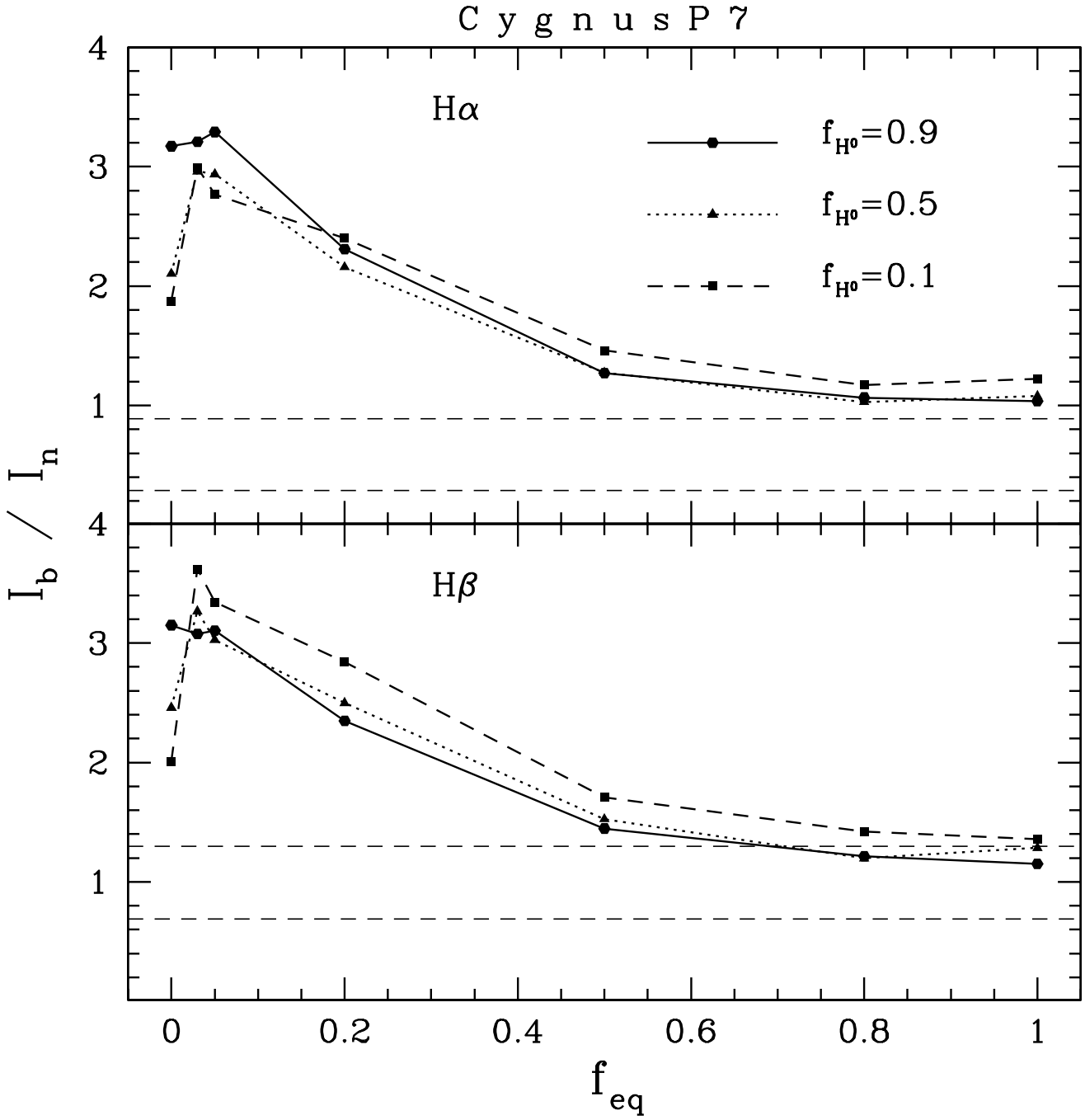
C y g n u s P 7
Hα
Hβ
f_{H^0}=0.9
f_{H^0}=0.5
f_{H^0}=0.1
I_b / I_n
f_{eq}
0
0.2
0.4
0.6
0.8
1
1
2
3
4

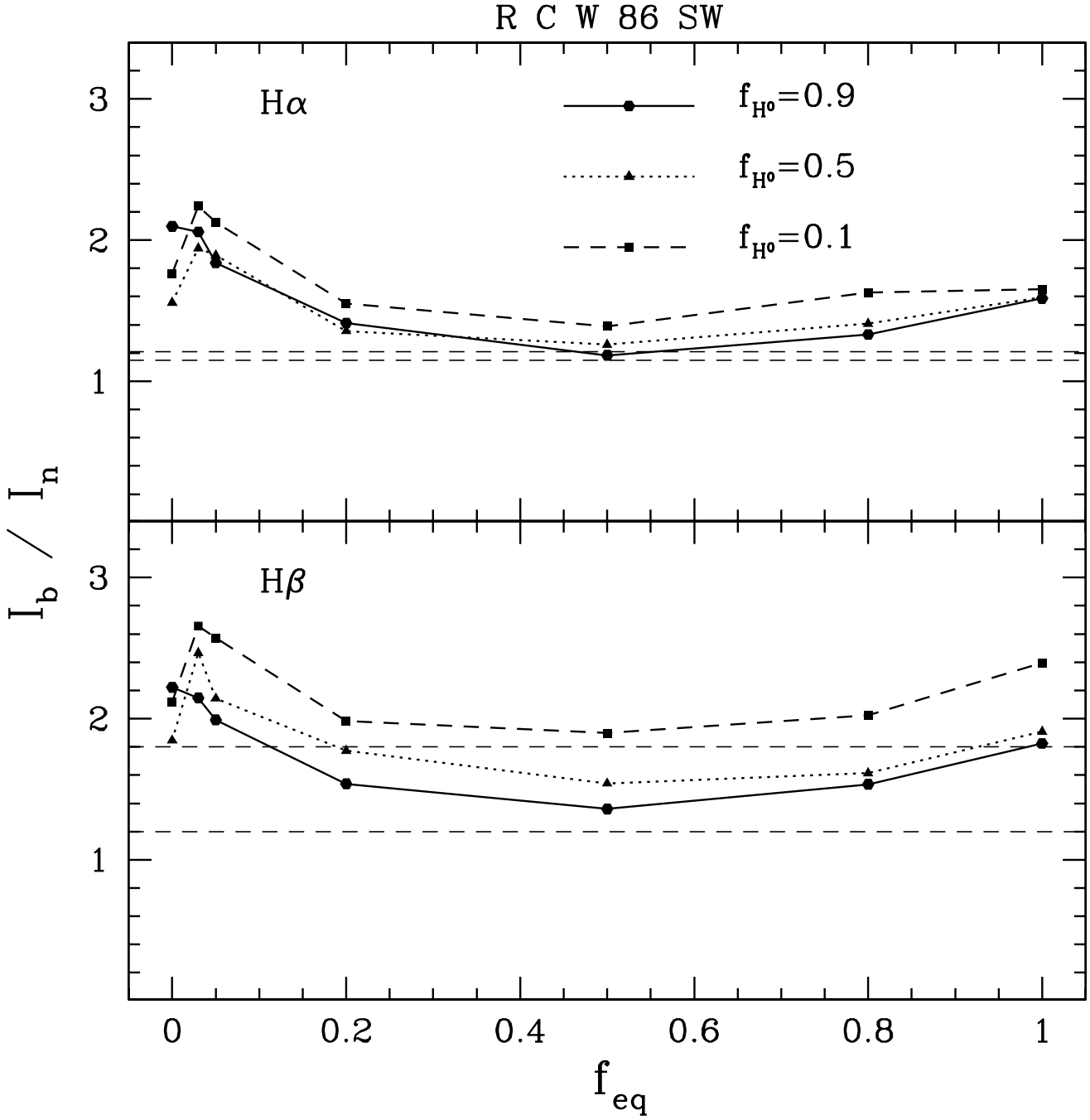
R C W 86 SW
Hα
Hβ
f_{H^0}=0.9
f_{H^0}=0.5
f_{H^0}=0.1
I_b / I_n
f_{eq}
1
2
3
0
0.2
0.4
0.6
0.8
1

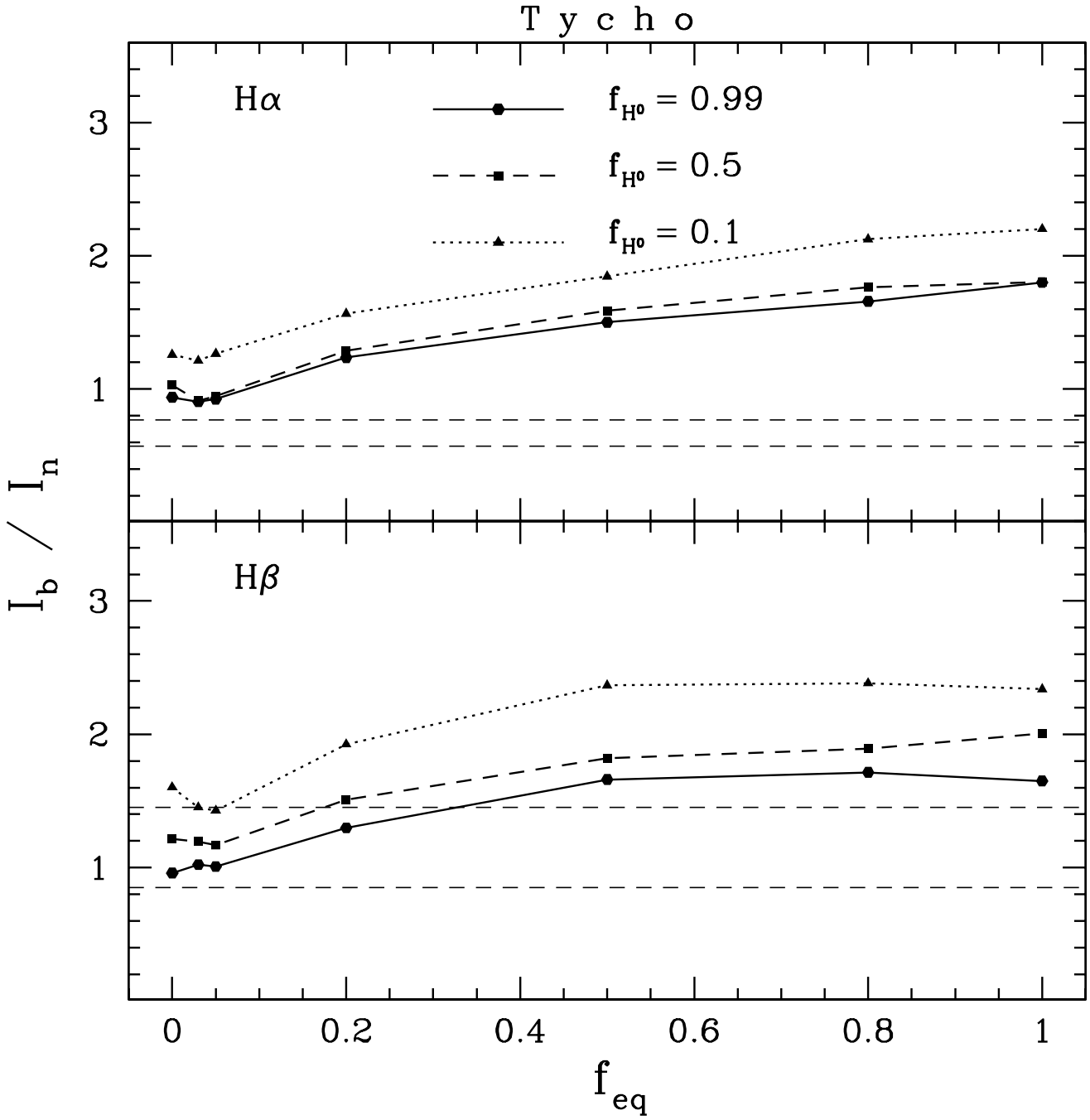
T y c h o
Hα
Hβ
$f_{H^0} = 0.99$
$f_{H^0} = 0.5$
$f_{H^0} = 0.1$
$I_b \ / \ I_n$
f_{eq}
0
0.2
0.4
0.6
0.8
1
1
2
3